REVIEW

Subject category: ENGINEERING

Nanomechanics of graphene

Yujie Wei[1,3*], Ronggui Yang[2]*

[1]The State Key Laboratory of Nonlinear Mechanics (LNM), Institute of Mechanics, Chinese Academy of Sciences, Beijing, China, 100190

[2]Department of Mechanical Engineering, University of Colorado, Boulder, CO, USA, 80309

[3]School of Engineering Sciences, University of Chinese Academy of Sciences, Beijing, China,100049

*Emails: yujie_wei@lnm.imech.ac.cn; ronggui.yang@colorado.edu

Abstract

The super-high strength of single layer graphene has attracted great interests. In practice, defects resulted from thermodynamics or introduced by fabrication, naturally or artificially, play the pivotal role in the mechanical behaviors of graphene. More importantly, high strength is just one aspect of graphene's magnificent mechanical properties: Its atomic-thin geometry not only leads to ultra-low bending rigidity, but also brings in many other uniqueness of graphene in terms of mechanics in contrast to other carbon allotropes, including fullerenes and carbon nanotubes. The out-of-plane deformation is of 'soft' nature, which gives rise to rich morphology and is crucial for morphology control. In this review article, we aim to summarize current theoretical advances on describing the mechanics of defects in graphene, and the theory to capture the out-of-plane deformation. The structure-mechanical property

relationship in graphene, in terms of its elasticity, strength, bending, and wrinkling, with or without the influence of imperfections, are presented.

Keywords: graphene, strength, wrinkling, pentagon-heptagon rings, carbon honeycomb

1. Introduction

There exist many reviews on the synthesis, properties and applications of graphene, and it has not been our purpose merely to add one to the many. Our aim is to demonstrate the mechanics of graphene as an integral part of materials and structures other than the isolated domain of remarkable individuals. This purpose demands more account of general mechanical analysis. We have found that this is particularly necessary as a general reader cannot be assumed to be comfortable with the applicability of classical mechanics theories to the mechanics of graphene.

Until the success of Geim and co-workers in producing monolayer graphene by mechanical exfoliation of graphite [1, 2], atomically thin materials were believed to be thermodynamically unstable under the ambient conditions [3, 4]. The emergence of graphene leads to great attention to examine its specialty in contrast to other carbon allotropes including fullerene, carbon nanotube, and graphite [5]. Among nearly 356 carbon allotropes from 500 scientific reports [6], the aforementioned carbon structures including fullerene, carbon nanotube, and graphene, are composed of single layer of carbon atoms. As both carbon nanotubes and graphene are composed of sp^2-bonded carbon atoms packed in a honeycomb crystal lattice, it is not surprise that graphene also has extremely high modulus and high strength as the well-studied carbon nanotubes [7-9]. What makes graphene distinct from carbon nanotubes is the two-dimensional structure and can be synthesized as large-area flat sheets, which opens up many applications that carbon nanotubes cannot be conveniently utilized.

The atomic-thin nature of graphene leads to its ultra-low bending rigidity, making it 'soft' for out-of-plane deformation. Graphene can be easily bent to form rich three-dimensional morphology [10-12] under either mechanical or thermal undulation. The bending properties accounting for rippling of graphene has been investigated. Also due to the increased surface area, the interaction between graphene and other materials has been studied. Typical mechanical behaviors involving surface interaction including adhesion [13, 14], peeling while transfer [15-17], as well as the frictional behavior [18-21] had drawn the attention of broad engineering communities. Small-size two-dimensional structures have edges, and those edges introduce mechanical complications and excitements [22]. Large area graphene usually consists of patches of small area graphene with different size and orientation, coupling with grain boundaries (GBs) and other defects [23-27]. The mechanics of those typical defects in graphene and their influence on the strength are also covered in this review. In short, the aim of this review article is to provide a comprehensive summary on the up-to-date progress on the mechanics of graphene, and more importantly, how to understand the relationship between structures and mechanical properties, with and without defects.

There are already several review papers in literature covering different aspects of the mechanics of two-dimensional (2D) materials. For example, the fracture of graphene has been reviewed by Teng et al. [28] where the authors summarized the recent progresses in experimental and theoretical studies on the fracture behaviors of graphene, and also presented significant yet unresolved issues related to the fracture of graphene. In the review by Cao et al. [29], the authors showed recent advance on the characterization of the mechanical behavior of atomically thin films. The review by Ivanovskii [30] generalized the information on the modification of graphene-based carbon materials through creation of structural defects, introduction of substitutive impurities, adsorption of impurity atoms and mechanical deformations. Several mechanical properties including elastic constants, strength, friction, and fracture of graphene have been included. A particular review on the tribology of graphene was given by Penkov et al. [31]. Recently Akinwande et al. [32] reviewed the mechanical properties of graphene and 2D materials. Penev et al. [33] reviewed the development of theoretical and computational model on the role of certain transcending concepts like elastic

instabilities, dislocations, and edges. CastroNeto et al. published a review paper [34] on the unusual two-dimensional Dirac-like electronic behavior of graphene, where the effects of electron-electron and electron-phonon interactions in single layer and multilayer graphene are presented. Ando [35] gave a review on the characteristic features of electronic states and electrical transport in both graphene and carbon nanotubes. A series of review papers on the chemical properties of typical 2D materials could be found in [36-39] and references therein. Wu et al. [40] reviewed up-to-date advances in graphene-based micro-electrochemical energy-storage devices which utilized the unique features of graphene and foresaw the future development of graphene based micro-supercapacitors. The thermal conductivity of 2D materials was reviewed by Gu et al. [41], where the effects of different physical factors, such as sample size, strain, and defects, on thermal transport in 2D materials are summarized.

2. Elasticity of pristine graphene

Because of the rich bonding types, different carbon allotropes show a large variety of elastic properties. Even being the same type of honeycomb lattice of carbon atoms, graphene and carbon nanotubes can exhibit quite different mechanical behaviors as they are categorized as typical examples of 2D and one-dimensional (1D) materials, respectively. In particular, the difference in the dimensionality of those allotropes gives rise to different degrees of freedom in response to external stimuli. For instance, while the in-plane elastic properties of pristine graphene could be largely inferred from that of the well-studied CNTs, the out-of-plane deformation mode in graphene requires a different theoretical tool. Here we introduce the available theoretical approaches to analyze the elastic response in graphene.

2.1 Two-Dimensional long-range crystalline order

For a long time, two-dimensional crystals have been conceived as structurally unstable because of long wavelength fluctuations according to the Mermin-Wagner theorem [42]. Two-dimensional crystals are extremely flexible and are prone to structural instability, which gives rise to microscopic corrugations of a graphene sheet [3, 4]. Nearly one century ago, Peierls [43] and Landau concluded that there can be no one- or two-dimensional long-range crystalline order. The argument given by Peierls is qualitative based on the harmonic

interaction of atoms in the one-dimensional chain. Landau's conclusion on the no existence of two-dimensional long-range crystalline order is based on his general theory of second-order phase transition [44], which is known to be misleading near the critical point. Alder and Wainright investigated a two-dimensional system consisting of 870 particles placed in a periodically rectangular array. Their computer experiments, however, have indicated a transition to a two-dimensional crystalline ordered state [45]. The theoretical analysis by Mermin a few years later [3] excluded long-range crystalline order in two dimensions for power-law potentials of the Lennard-Jones type, but it is inconclusive for other types of potentials. The conclusion was made by deriving the Fourier component of the density for each vector of the reciprocal lattice. Considering a two-dimensional crystalline flake with the Bravais lattice ascribed by $\vec{\boldsymbol{a}}$ and $\vec{\boldsymbol{b}}$ where the flake sides are defined by $N_1\vec{\boldsymbol{a}}$, $N_2\vec{\boldsymbol{b}}$. An arbitrary lattice point is defined by $\vec{\boldsymbol{r}} = m\vec{\boldsymbol{a}} + n\vec{\boldsymbol{b}}$, $m, n = 0,1, \dots, N_1$. The total number of atoms in the flake is then $N = cN_1N_2$, where c is the number of atoms in the unit cell defined by $\vec{\boldsymbol{a}}$ and $\vec{\boldsymbol{b}}$. The real space density distribution is simply given by

$$\hat{\rho}(\vec{\boldsymbol{r}}) = \sum_{i=1}^{N} \delta(\vec{\boldsymbol{r}} - \vec{\boldsymbol{r}}_i). \qquad (1)$$

In the reciprocal space, the *k*-th component of the Fourier's transform of the real space is obtained as

$$\hat{\rho}(\vec{\boldsymbol{k}}) = \int \hat{\rho}(\vec{\boldsymbol{r}}) \mathrm{e}^{-\mathrm{i}\vec{\boldsymbol{k}}\cdot\vec{\boldsymbol{r}}} d\vec{\boldsymbol{r}} = \sum_{i=1}^{N} \mathrm{e}^{-\mathrm{i}\vec{\boldsymbol{k}}\cdot\vec{\boldsymbol{r}}_i}. \qquad (2)$$

The integration is over all the atoms in the flake. By defining the *k*-th Fourier's component of the density

$$\rho_{\vec{\boldsymbol{k}}} = \frac{1}{N}\langle\hat{\rho}(\vec{\boldsymbol{k}})\rangle, \qquad (3)$$

with $\langle\cdots\rangle$ an averaging of density in the reciprocal space

$$\langle\hat{\rho}(\vec{\boldsymbol{k}})\rangle = \int \frac{\hat{\rho}(\vec{\boldsymbol{k}})\mathrm{e}^{-\mathrm{U}(\vec{\boldsymbol{r}}_1,\vec{\boldsymbol{r}}_2,\dots,\vec{\boldsymbol{r}}_N)/kT} d\vec{\boldsymbol{r}}_1 \dots d\vec{\boldsymbol{r}}_N}{\int \mathrm{e}^{-\mathrm{U}(\vec{\boldsymbol{r}}_1,\vec{\boldsymbol{r}}_2,\dots,\vec{\boldsymbol{r}}_N)/kT} d\vec{\boldsymbol{r}}_1 \dots d\vec{\boldsymbol{r}}_N}, \qquad (4)$$

where kT is the product of the Boltzmann constant and the absolute temperature with the unit Kelvin (K). Atoms in the flake interact through the pair potential $\Phi(\vec{\boldsymbol{r}})$, and we hence have the expression of internal energy $\mathrm{U}(\vec{\boldsymbol{r}}_1, \vec{\boldsymbol{r}}_2, \ldots, \vec{\boldsymbol{r}}_N) = \frac{1}{2}\sum_{i \neq j} \Phi(\vec{\boldsymbol{r}}_i - \vec{\boldsymbol{r}}_j)$. For an entirely crystalline object, it stands to reason that there is an array of sharp peaks in reciprocal space and $\rho_{\vec{\boldsymbol{k}}}$ will be non-zero. Mermin [3] adopted as criterion for the existence of thermodynamically periodic arrangement of atoms in the flake the following: $\lim_{N_1,N_2\to\infty} \rho_{\vec{\boldsymbol{k}}} \neq 0$ if $\vec{\boldsymbol{k}}$ is a reciprocal-lattice vector, and $\lim_{N_1,N_2\to\infty} \rho_{\vec{\boldsymbol{k}}} = 0$ for other case of $\vec{\boldsymbol{k}}$. He gave a proof that the first case cannot be satisfied in two dimensions for $\Phi(\vec{\boldsymbol{r}})$ being power-law potentials of the Lennard-Jones type, but it is inconclusive for other types of potentials [3]. In 2002, Ab initio calculations showed that a graphene sheet is thermodynamically unstable if its size is less than about 20 nm and becomes the most stable fullerene only for molecules larger than 24,000 atoms [46].

The success of Geim and co-workers to produce the monolayer graphene by mechanical exfoliation of graphite [1, 2] ended the theoretical controversy on thermodynamically stable two-dimensional crystals under the ambient conditions. Now many one-atom thin and multi-atom thin 2D materials were discovered with exploded literature studying their synthesis, physical properties, and applications. While large-area pristine graphene may not be flat under thermal undulation [11], it can resist bending and remains two-dimensional, in particular when the size of a graphene flake is small. It should be pointed out that the sp^2 bonding among carbon atoms in graphene certainly deviates from the power-law inter-atomic potential assumed in the theoretical analysis by Mermin [3]. In that sense, Mermin's analysis does not exclude the existence of stable two-dimensional crystals with interactions significantly different from the Lennard-Jones type of potentials.

Very recently, Kumar and Parks [47] further analyzed the lattice dynamic stability of graphene under straining, and deduced a general continuum criterion for the onset of various kinds of lattice instabilities in graphene: an instability appears when the magnitude of the deviatoric strain γ reaches a critical value γ_c, which depends on the mean normal strain and the directionality θ of the principal deviatoric stretch with respect to the reference lattice

orientation. The criterion could be employed to distinguish fundamentally different mechanisms of lattice instabilities in graphene, such as structural versus material instabilities, and long-wave (elastic) versus short-wave instabilities.

2.2 In-plane elasticity

Given the atomic-thin nature, how two-dimensional crystals resist deformation is of paramount interest. In this subsection, we first examine the in-plane elastic properties of single layer graphene. As imagined, graphene is the mother element of some carbon allotropes including CNTs [48, 49]. Naturally, the same lattice in graphene and CNT may be expected to have similar elasticity. The distinction originates from the structures. The elastic modulus of CNT is normally an effective one from the structure level: the stress is typically averaged over the circular cross-section of the tube. It is an effective modulus which may depend on the chirality of the CNT. For graphene, we consider the most general case regarding the mechanical response of graphene with the honeycomb lattice.

It is known that the change in the free energy F in an anisotropic crystal under small deformation can be described by a quadratic function of the strain (in the Cartesian coordinate) [5]:

$$F = \frac{1}{2} c_{ijkl} \varepsilon_{ij} \varepsilon_{kl}, \qquad (5)$$

where i, j, k, l are integers ranging from 1 to 3, and ε_{ij} are strain components. The coefficient c_{ijkl} is the rank-four elastic modulus tensor, including a maximum of 21 independent components for the triclinic system, but fewer in the crystals possessing symmetry. For hexagonal systems like graphene, their normal plane is the sixth-order axis: rotating through an angle of $\pi/3$ about the plane normal results in the exact same lattice. The free energy is hence simplified as

$$F = \frac{1}{2} c_{3333} \varepsilon_{33}^2 + 2c_{1212} (\varepsilon_{11} + \varepsilon_{22})^2 + c_{1122} [(\varepsilon_{11} - \varepsilon_{22})^2 + 4\varepsilon_{12}^2] + 2c_{1233} \varepsilon_{33} (\varepsilon_{11} + \varepsilon_{22}) + 4c_{1223} (\varepsilon_{13}^2 + \varepsilon_{23}^2). \qquad (6)$$

From eqn. (6), we can see that five-independent elastic moduli are needed to describe the elastic deformation of a hexagonal crystal. When only the in-plane deformation is considered, i.e., $\varepsilon_{i3} = 0$ for $i = 1 \cdots 3$, the free energy is determined by the two elastic constants c_{1212} and c_{1122} in eqn. (6). It hence suggests that the elastic behavior of two-dimensional hexagonal crystals like graphene is isotropic in nature, consistent with other explorations [50].

The isotropic elastic property of a hexagonal lattice can be alternatively understood at a macroscopic level if we take an analogy between the lattice and the honeycomb structure [51]. In the most general case, deformation in the $X_1 - X_2$ plane in a honeycomb composed of unit cells shown in Figs. 1a and b is described by five moduli: two Young's moduli E_1 and E_2, the shear modulus of G_{12}, and two Poisson's ratios ν_{12} and ν_{21}. But there are only four independent ones as the reciprocal relation requires $E_1\nu_{21} = E_2\nu_{12}$. The two moduli are thus given, respectively, as

$$\frac{E_1}{E_w} = \left(\frac{t}{L}\right)^3 \frac{\cos\theta}{(h/L+\sin\theta)\sin^2\theta} \qquad (7a)$$

and

$$\frac{E_2}{E_w} = \left(\frac{t}{L}\right)^3 \frac{h/L+\sin\theta}{\cos^3\theta}, \qquad (7b)$$

where E_w is the Young's modulus of the wall material. It is convenient to see that for a hexagonal lattice, we have $E_1 = E_2$. The Poisson's ratio, for loading along X_1-direction, is given as

$$\nu_{12} = \frac{\cos^2\theta}{(h/L+\sin\theta)\sin\theta}, \qquad (7c)$$

and that is

$$\nu_{21} = \frac{(h/L+\sin\theta)\sin\theta}{\cos^2\theta} \qquad (7d).$$

when loading along X_2-direction.

Again in a hexagonal lattice, we see $\nu = \nu_{12} = \nu_{21} = 1$ for $\theta = 30°$ and $h/L = 1$. The shear modulus of the honeycomb is thus,

$$\frac{G_{12}}{E_w} = \left(\frac{t}{L}\right)^3 \frac{h/L+\sin\theta}{(h/L)^2(2h/L+1)\cos\theta}. \quad (7e)$$

In the case of an ideal hexagon lattice, we also have the relation of $G_{12} = \mathrm{E}/2(1+\nu)$, which generally applies for isotropic solids. While there are apparent discrepancies between the hexagonal lattice like graphene and the hexagonal honeycomb as bending is considered to be the primary mechanism for elastic deformation for honeycombs, the comparison of the two systems can help us understand the isotropic nature of the in-plane mechanical properties in graphene under small deformation. When the deformation becomes large and the unit cell is severely distorted, changes in θ and h/L would consequentially render the system to be anisotropic. This observation may explain the nonlinear behavior of graphene during the elastic stage [52] and the slight anisotropic mechanical properties reported in the literature.

Aside from the topological difference, single wall carbon nanotubes have the same lattice structure as that of graphene. Hence, the tensile behavior of graphene can essentially be deduced from those of carbon nanotubes, as long as the tube radius is not too small. For example, VanLier et al. reported the Young's modulus and the Poisson ratio for a number of closed single-wall carbon nanotubes using the first all-electron *ab*-initio calculation [53]. The results agree well with those of graphene. Typical theoretical analysis predicts a Young's modulus of graphene to be higher than 1 TPa. The Poisson ratio in graphene is found to be small, close to 0.1 in a broad range of temperatures [54]. Liu et al. [52] calculated the phonon spectra of graphene as a function of the uniaxial tension by the density functional perturbation theory (DFPT) to assess the first occurrence of phonon instability on the strain path, which controls the strength of a defect-free crystal at 0 K. They obtained a Young's modulus E=1050 GPa and Poisson's ratio ν=0.186 from small-strain calculations.

2.3 In-plane nonlinearity

In the first effort to measure the break strength of graphene (Fig. 1c), Lee et al. [7] employed the indentation tests and found that the maximum stress attained in the film agreed well with an analytical solution [55] when a linear stress-strain curve is employed. To match the load-deflection curve as shown in Fig. 1d, however, the strains in the graphene near the

indenter had to be set to values well over 0.2, which is far beyond the linear elastic regime. The stress-strain curves along different loading directions do show nonlinearity and large break strain (see Fig. 1e). Therefore, a non-linear elastic constitutive behavior [56] has to be adopted by counting the higher order strain terms in the strain energy density formula [55]:

$$F = \frac{1}{2} c_{ijkl} \varepsilon_{ij} \varepsilon_{kl} + \frac{1}{2} D_{ijklmn} \varepsilon_{ij} \varepsilon_{kl} \varepsilon_{mn}, \quad (8)$$

where D_{ijklmn} are the third-order elastic moduli. Casting this relationship in a uniaxial strain context, Lee et al. [7] wrote the stress, σ, and strain, ε, relationship as $\sigma = E\varepsilon + D\varepsilon^2$. Such a relationship captures reasonably well the nonlinear response of the indentation force vs. depth curves from their experiments. The same technique was also adopted later for measurement of the strengths of the grain boundaries in graphene [9] and graphene oxide [8]. Cadelano et al. [57] discussed the physical meaning of the effective nonlinear elastic modulus. The authors developed the constitutive nonlinear stress-strain relation for graphene, and predicted its value to be in good agreement with available data in literature. It is essential to use a physically sound constitutive model to capture the nonlinear region in the stress-strain curves, although another issue, the anisotropic failure strength of graphene [58], has been largely ignored in the existing analysis.

2.4 Out-of-plane deformation

In contrast to its in-plane deformation, the out-of-plane deformation which is peculiar to the one-atom thin graphene is of importance. Carbon atoms restricted to a finite-size surface closure like a sphere (fullerene) or a tube (CNT) can behave very differently from graphene flakes that are essentially flat. A free-standing graphene can easily be bent under thermal undulation [11]. Pivotal to this are the two mechanical parameters - bending rigidity and Gaussian bending stiffness - which govern the morphology of graphene under external stimuli. The structure and morphology manipulation, on the other hand, are broadly investigated for the potential applications of graphene in biological systems and stretchable electronics [59].

2.4.1 Bending stiffness

A reliable characterization of bending rigidity and Gaussian bending stiffness of graphene is of significance for both the design and the manipulation of graphene morphology for engineering applications. It may be interesting to see first the prediction from the continuum mechanics, although there are always concerns about the applicability of the continuum theories for predicting the mechanical properties of graphene or carbon nanotubes (CNTs). Based on the Kirchhoff–Love theory, the bending stiffness of thin plates is determined as

$$B_M = \nu_{12} = \frac{EH^3}{12(1-\nu^2)}, \qquad (9)$$

where E is the Young's modulus, ν is the Poisson's ratio, and with H is the the thickness of the thin plate. For graphene, we have E =1050GPa, and υ=0.186 [60-62]. The thickness H is where most controversies originated from. If one extrapolates the graphene thickness by counting its stacking in the crystalline graphite, we have H = 0.34 nm. Substituting this number H = 0.34 nm into eqn. (9) yields B_M=22.3eV, which is significantly larger than the measured value [63]. The break-down of the applicability of the continuum theory to predict the bending properties in graphene suggests that H may not be 0.34nm for a single layer graphene while a smaller effective thickness might reconcile the difference for B_M between the prediction by the continuum mechanics theory and the experimental value.

Instead of applying the continuum mechanics theory to calculate the bending stiffness of the low-dimensional carbon nanostructures, atomistic simulations have also been broadly used to predict the mechanical behaviors of small structures and systems. Wei et al. [59] applied the density functional theory (DFT) calculations to obtain the energies of zero-dimensional fullerenes and one-dimensional single wall carbon nanotubes (SWCNTs) of different radii, and then derived both the bending rigidity and the Gaussian bending stiffness of free-standing single layer graphene (Fig. 2a).

By combining the density functional theory calculations of energies of fullerenes and single wall carbon nanotubes with the configurational energy of membranes determined by the Helfrich Hamiltonian [64, 65], Wei et al. [59] designed a theoretical approach to

accurately determine the bending rigidity and Gaussian bending stiffness of single-layer graphene. For a membrane with three-dimensional topology, the configurational energy ψ_H described by the Helfrich Hamiltonian [64, 65] as:

$$\psi_H = \int_S [\gamma + 2B_M(C_M - C_0/2)^2 + B_G C_G]\, ds, \qquad (10)$$

where γ is the energy for unitary flat surface, B_M is the flexural stiffness (bending rigidity), B_G is the Gaussian bending stiffness, $C_M = (k_1 + k_2)/2$ is the mean curvature whereas k_1 and k_2 are the two principal curvatures of a three-dimensional surface, $C_G = k_1 k_2$ is the Gaussian curvature, and C_0 is spontaneous curvature, which disappears for symmetrical membranes. The integral in eqn. (10) extends over the whole surfaces.

Considering single layer graphene as a membrane, the surface energy γ remains to be constant during pure bending. By utilizing the fact that SWCNT can be rolled up from a graphene [5], in graphene the term associated with the Gaussian curvature disappear. By varying the radius of SWCNTs, one would then find that the energy per atom in SWCNT can be related to the energy per atom in graphene with the radii of SWCNTs by

$$E_{atom}^{CNT} = E_0 + S_0 \frac{B_M}{2r^2}, \qquad (11)$$

where *r* is the radius of SWCNTs, E_{atom}^{CNT} is the energy per atom in a SWCNT, E_0 is the energy of an atom in a flat graphene, and $S_0 = 3\sqrt{3}d^2/4 = 2.63\text{Å}^2$ is the planar footprint (area) of a carbon atom in graphene with *d* being the C-C bond length. By calculating the energy per atom in SWCNTs with different radii, it is straightforward to derive the bending rigidity of graphene using eqn. (11). To determine the Gaussian bending stiffness B_G, a series of spheroidal fullerenes with total atom numbers from 60 to 540 are considered, which have a corresponding radius variation from 1.86 Å to about 11 Å. Using eqn. (10), the energy per atom in fullerenes can be given as

$$E_{atom}^{F} = E_0 + S_0 \frac{2B_M + B_G}{r^2}. \qquad (12)$$

With B_M known using eqn. (11), B_G in eqn. (12) could then be determined. The bending rigidity and Gaussian bending stiffness of single-layer graphene are 1.44eV (2.31×10^{-19}Nm) and -1.52eV (2.43×10^{-19}Nm), respectively. The bending rigidity from this model is close to the measured result.

2.4.2 Correlation between the two bending stiffness

The relationship between the bending rigidity and the Gaussian bending stiffness in graphene is intriguing. The graphene sheet may be treated classically as an elastic plate and the solutions to the bending deformation of thin plates can be adopted. Assuming isotropic and homogeneous, and following Timoshenko and Woinowsky [66], the differential equation of the deflection z of a graphene sheet is given as

$$\frac{\partial^4 z}{\partial x^4} + 2\frac{\partial^4 z}{\partial x^2 \partial y^2} + \frac{\partial^4 z}{\partial y^4} = \frac{q}{B_M}. \qquad (13)$$

where q is the distributed load normal to the surface. By neglecting the contribution of the shearing stress on the deflection of the graphene, its total energy is then given as

$$\psi = \frac{1}{2}B_M \int \left\{ \left(\frac{\partial^2 z}{\partial x^2} + \frac{\partial^2 z}{\partial y^2}\right)^2 - 2(1-\nu)\left[\frac{\partial^2 z}{\partial x^2}\frac{\partial^2 z}{\partial y^2} - \left(\frac{\partial^2 z}{\partial x \partial y}\right)^2\right]\right\} dx\, dy, \qquad (14),$$

where the integration is extended over the entire surface of the graphene.

Recognizing that

$$(k_1 + k_2) = -\left(\frac{\partial^2 z}{\partial x^2} + \frac{\partial^2 z}{\partial y^2}\right) \qquad (15a)$$

and

$$(k_1 k_2) = \frac{\partial^2 z}{\partial x^2}\frac{\partial^2 z}{\partial y^2} - \left(\frac{\partial^2 z}{\partial x \partial y}\right)^2, \qquad (15b),$$

we may split the energy terms in eqn. (14) into the bending and the twisting contributions, respectively. By substituting the two terms in eqn. (15) into eqn. (14) and then making a comparison with eqn. (10), the following relationship between B_M and B_G for thin plates is obtained,

$$\frac{B_G}{B_M} = \nu - 1. \qquad (16).$$

Recalling that the Poisson ratio in graphene is found to be small, approximate to 0.1 in a broad temperature range [54], we will have a $\frac{B_G}{B_M}$ ratio about - 0.9. If eqn. (16) is applied to graphene, we found that the prediction roughly matches with the results from DFT calculations [59].

In the classical theory, the value of acceptable Poisson ratio should be positive. Yu and Ru [67] showed that when the ratio of the Gaussian bending rigidity to the common flexural rigidity falls within the non-classical range, actual mechanical behavior of such a membrane with two independent bending rigidities could be very sensitive to the exact values of the two independent bending rigidities and hence the Poisson ratio. Recently, Davini et al. [68] considered a discrete model of a graphene sheet with inter-atomic interactions governed by the harmonic approximation of the 2nd-generation Brenner potential, which depends on bond lengths, bond angles, and two types of dihedral angles. The authors proposed an analytical expression for the Gaussian stiffness, which turns out to be in good agreement with the DFT calculations. It was revealed recently [69] that the thermal fluctuations of elastic sheets can affect the effective bending stiffness at finite temperatures. Zhang et al. [70, 71] demonstrated controllable out-of-plane wrinkles by utilizing the ultra-low bending stiffness of graphene and topological defects. Boddeti et al. [72] demonstrated that graphene blisters with switchable shapes could be realized by controlling pressure and adhesion, where both stiffness play a governing role for morphology stability.

2.5 Edge effects

One of the most significant geometrical features of graphene is the unprecedented surface area to volume ratio owing to the nature of one-atom-thickness. The ultra-low bending resistance of such thin layers makes it difficult to control their morphology. Furthermore, the presence of edges in graphene nanostructures gives rise to rich morphology change due to the non-equilibrium edge atoms. With an aberration-corrected transmission electron microscope with both atomic-scale spatial resolution and 1-second temporal resolution, Girit et al. [73]

observed the dynamics of carbon atoms at the edge of a single layer graphene. The detailed edge reconstruction and the stability of the "zigzag" edge configuration were reported. The results of the *ab initio* calculations of the effect of reconstruction and passivation of zigzag edges demonstrated that hydrogen-passivated ideal zigzag edges are more energetically favoured than the pentagon-heptagon zigzag edges. However, the reconstructed edge is more stable in the absence of hydrogen [74]. At high temperature and low (quasi-static) mechanical loading rate [75] it is possible to obtain fully reconstructed zigzag edges through sequential reconstructions at the crack tip during the fracture of graphene.

The success in making graphene ribbons (GNR) with nanoscale widths on the order of tens of nanometers [76-80] boosts the research in understanding the morphologies of those nanostructures [81], in addition to the theoretical predictions that the edge states in GNR lead to the size effects on the electronic state of graphene for being metallic, insulating, or semiconducting [82, 83]. Point defect annealing and edge reconstruction during edge-reconstruction process lead to ribbon morphology patterning and distinct physical properties resulted from local edge structure [80]. When the electron and phonon mean free paths are comparable to or even greater than the ribbon widths, electron and phonon transport can be altered dramatically [84-86]. A number of studies reported the ballistic, hydrodynamical, and even rectified phonon transport in graphene nanoribbons after Hu et al. [87]. Ritter and Lyding [88] used a tunnelling spectroscopy to show that the electronic structure of GNRs with 2-20 nm width varies on the basis of the graphene edge lattice symmetry. GNRs with a higher fraction of zigzag edges exhibit a smaller energy gap than a predominantly armchair-edge ribbon of similar width. Zhang et al. [89] reviewed the chemical properties in graphene edges, especially the catalyst-passivated graphene edges and their role in graphene CVD growth. Kim et al. [90] experimentally demonstrated that folded structures in graphene could be realized by introducing anisotropic surface curvature during graphene synthesis or material transfer processes, and consequentially modifies the electronic band structure of graphene.

Distinct bonding characteristics of atoms at the free edges of GNR may introduce excessive edge energy and edge force which are also chiral dependent [91-96]. Shenoy et al. [91] demonstrated that edge stresses could introduce intrinsic ripples in a free-standing

graphene sheet even in the absence of any thermal effects. Compressive edge stresses along the zigzag and the armchair edges of the sheet can cause out-of-plane warping to attain several degenerate shape modes. Cranford and Buehler [97] developed a mesoscopic two-dimensional model for a graphene sheet utilizing coarse-grain bead-spring elements with rotational-spring potentials. The authored used their mesoscopic model to study the structure and conformational behavior of twisted ultra-long multilayer graphene ribbons with lengths of hundreds of nanometers. They even revealed a distinct transition from a twisted (saddle-like) configuration to a helical (coil-like) configuration as a function of the imposed rotation and number of graphene layers.

Deformation of GNRs is driven by the excess energy in the presence of edges and the subsequent edge stress. The mechanical deformation of a free-standing GNR could be modeled as a long membrane, with edges represented by elastic strings either in an elongated or compressed state and glued to the long edges of the membrane. Taking an analogue between the edge stress of a 2D membrane and surface stress of a 3D bulk solid, Shenoy et al. [91] wrote the energy per unit length of a GNR with width W as

$$\mathcal{F}(w,\varepsilon) = \frac{1}{2}EW\varepsilon^2 + 2\Gamma_e\varepsilon + E_e\varepsilon^2 + \mathcal{F}_0, \qquad (17)$$

where Γ_e denotes the edge stress, and E_e is the elastic moduli of the edges, and $\mathcal{F}_0$ is the reference energy state. To understand the edge-stress-driven warping in graphene nanoribbons, Shenoy et al. [91] considered a two-dimensional half-space, $-\infty < x_1 < +\infty$ and $0 \le x_2 < +\infty$. The authors used the perturbation strategy by assuming the out-of-plane deflection z is in the form of

$$z = Asin(kx_1)e^{-x_2/l}, \qquad (18)$$

where k is the wave number and the characteristic wave penetration depth is l. In the edge ($x_2 = 0$), the periodic rippling size is $\lambda = 2\pi/k$ and the amplitude of the ripples is A. The strain components of in the GNR could hence be given as [98]

$$\epsilon_{ij} = \frac{1}{2}\left(\frac{\partial u_i}{\partial x_j} + \frac{\partial u_j}{\partial x_i}\right) + \frac{1}{2}\frac{\partial z}{\partial x_i}\frac{\partial z}{\partial x_j}. \qquad (19)$$

It is noted that the first term of the right hand side in the eqn. (19) comes from the in-plane displacement (u_1, u_2), and this part is usually neglected due to its relatively small contribution to the overall deformation and the strain energy. For compressive edge stresses, warping in the edges is a favorable configuration with lower free energy. The free-energy density associated with different deformation modes, as seen in eqn. (17), could then be deduced. The wave penetration depth is then deduced by using the energy minimization criterion and is related to λ as $l = 0.23\lambda$, and the most-probable amplitude of edge ripples is [91]

$$A = \left[\frac{-\lambda\Gamma_e}{\left(\pi\sqrt{20+14\sqrt{7}}\right)\frac{E}{18(1-\nu^2)}+\frac{3\pi^2}{2\lambda}E_e}\right]^{0.5}, \qquad (20)$$

Indeed, molecular dynamics simulations with the Adaptive Intermolecular Reactive Empirical Bond Order (AIREBO) potential [99] as implemented in the software package LAMMPS [100] have been used to predict the compressive edge stresses in GNR. The values are 10.5 and 20.5 eV/nm in the armchair and zigzag edges, respectively. The predicted penetration depth and rippling amplitude are in good agreement with the corresponding results from MD simulations, as shown in (Figs. 2b to d). A combination of edge stress and the low bending resistance of GNR could be utilized to make complex folding structures, as demonstrated in Fig. 2e by Kim et al. [90]. Figures 2f to h showed cutting-edge experiments to monitor mechanical vibrations in suspended graphene sheets [101].

It is worth pointing out that several important factors were not considered in the theoretical analysis summarized in eqns. (17) to (19): (1) In reality, a GNR is of finite width. The finite width, in particular when a GNR is only several nanometers in width, could not be captured by the analysis based on semi-infinite two-dimensional space. As revealed by Lu and Huang [102], for graphene nanoribbons of width less than the intrinsic wavelength, interaction between the two free edges becomes significant, leading to anti-phase correlation of the buckling waves. (2) Temperature is found to play an important role in the rippling of graphene which is called thermal undulation. The edge stress is also a function of temperature. (3) The competition of rippling by thermal undulation with edge stress-driven

rippling would lead to some more interesting phenomena. Dewapriya and coauthors revealed that temperature, in combination with free edges, influences significantly the mechanical properties of graphene [103].

2.6 Strength and fracture of pristine graphene

We discuss in previous sections the elastic response of graphene. Beyond the elastic limit, a pristine graphene breaks in response to further tension. The stress at which graphene is torn apart characterizes the strength of graphene, and is another extraordinary property of this class of amazing two-dimensional materials.

2.6.1 Strength

Given the same chemical nature, the strength of single layer graphene is expected to be the same as that of carbon nanotubes if the edge effect is neglected, as confirmed by the very first experimental measurement on the strength of graphene. Lee et al. [7] measured the intrinsic strength of monolayer graphene by nano-indentation in an atomic force microscope. While it is not a standard tensile test to characterize the stress-strain response of materials, the authors extracted the stress-strain curve from the force-depth curve obtained from the indention tests. The inferred Young's modulus of E = 1.0 TPa and intrinsic strength of 130 GPa for monolayer graphene match reasonably well with the strength of single wall carbon nanotubes [10, 104, 105]. These experiments established the foundation that graphene is the strongest material ever measured. The measured strength of 130 GPa for graphene is about 20% higher than the calculated value by the density functional perturbation theory at 0 K.

The inferred strain in the graphene sheet directly beneath the diamond indenter at the measured failure load is anomalously large compared to the fracture strains predicted by both the soft-mode and the acoustic analyses. Liu et al. [52] calculated the phonon spectra of graphene as a function of uniaxial tension by the density functional perturbation theory to assess the first occurrence of phonon instability on the strain path, which controls the strength of a defect-free crystal at 0 K. The failure strength to break the zigzag plane (loading along armchair direction and the armchair plane (loading along zigzag direction) are 110 GPa and

121 GPa, respectively. This discrepancy, as further elaborated by [106], may originate from the strain-shielding effect initiated by mechanochemical interactions at the graphene–indenter interface. Transmission electron micrographs and a molecular model of the diamond indenter's tip together suggest that the tip surface contains facets comprising crystallographic {111} and {100} planes.

A more systematic study on the ideal tensile strength of pristine graphene as a function of the loading orientation by using the density functional theory (DFT) and energy minimization calculations was given by Yin et al. [58]. The detailed computational procedure has been described in reference [107]. By defining θ as the angle between the tensile loading direction (along *x*-axis) and the zigzag edge and σ_b the strength of an individual C-C bond, the critical stresses to break the zigzag plane is defined as

$$\sigma_c = \frac{\sigma_b}{\cos(60°+\theta)}. \qquad (21a)$$

Similarly, the critical stresses to break the armchair plane are

$$\sigma_c = \frac{2\sigma_b}{\cos\theta[\cos(30°+\theta)+\cos(30°-\theta)]}. \qquad (21b)$$

The required stress to break the zigzag plane and that to break the armchair plane at different angle θ differ significantly, with the latter being larger than the former. From the energy perspective, however, the zigzag plane should be harder to break as it has greater edge energy than that of the armchair plane [108]. This difference implies that one may need to distinguish the brittle fracture governed by the ideal strength with that by the edge energy.

2.6.2 Fracture

In the presence of cracks, graphene sheets typically break along the initial crack. A comprehensive review on the fracture behavior of graphene has been given by Teng et al. [28]. As there is no perceivable macroscopic plastic deformation in the stress-strain response of a graphene, graphene is believed to be brittle in nature, *i.e.*, the single layer graphene fractures at the nominal peak stress. It exhibits negligible plasticity till its failure at room temperature [8]. As discussed in Section 2.1, its elastic response is isotropic at small strain.

Here we focus on the directionality of fracture in graphene and its fracture toughness measurement.

According to the Griffith criterion, the critical fracture stress σ_f beyond which a pre-cracked isotropic stripe under mode I loading would extend is given as [109]:

$$\sigma_f = \frac{1}{F(\phi)}\sqrt{\frac{E\Gamma}{\pi a}}, \qquad (22a)$$

where E is Young's modulus, Γ is the apparent fracture resistance of the crack plane. In brittle materials, Γ is regarded as the surface energy for 3D materials and the edge energy for 2D materials. In eqn. (22), $F(\phi)$ is a geometrical factor given by [110]

$$F(\phi) = (1 - 0.025\phi^2 + 0.06\phi^4)\sqrt{\sec(\frac{\pi\phi}{2})} \quad \text{and} \quad \phi = \frac{W}{2a}, \qquad (22b)$$

where W is the width of the stripe with a central crack of length $2a$.

Both Γ and the critical crack size are of practical importance. Zhang et al. [111] measured the fracture toughness using a nanomechanical device in a scanning electron microscope. The fracture toughness of graphene was measured by obtaining the critical stress intensity factor of a pre-cracked graphene and then deducing its critical strain energy release rate to be $\Gamma = 15.9\ \mathrm{J}/m^2$. In contrast, the measured fracture toughness of the CVD-grown graphene by Hwangbo et al. [112] is about $K_C = 10.7{\sim}14\ \mathrm{MPa}\sqrt{m}$) and this number is higher than that from Zhang et al. [111]. Note that the two groups used different testing techniques: Zhang et al. [111] tested free-standing graphene using a micromechanical system while Hwangbo et al. [112] employed pressure bulge testing setup. Whether the difference came from the geometrical effects (e.g., possible rippling in the graphene during bulge tests will enlarge the apparent fracture resistance) remains to be explored with well-controlled experiments. Via a comparative *in situ* fracture toughness testing on single-edge V- and U-notched multilayer graphenes and boronitrenes BN) in a high-resolution transmission electron microscope (HRTEM), Wei et al. [113] reported that the fracture toughness of multilayer graphene and boronitrene to be $K_{IC} = 12 \pm 3.9\ \mathrm{MPa}\sqrt{m}$ and $K_C = 5.5 \pm 0.7\ \mathrm{MPa}\sqrt{m}$, respectively.

More recently numerical simulations showed that the fracture behaviour in graphene is orientation-dependent [114]. Table 1 gives the fracture resistance of graphene when the initial

crack is along different chirality. Here the orientation of a single layer graphene is described by two vectors $\boldsymbol{a}_1$ and $\boldsymbol{a}_2$, and the crack edge is described by a chiral vector $\boldsymbol{C}_h = n\boldsymbol{a}_1 + m\boldsymbol{a}_2$. The armchair and the zigzag directions correspond to $\boldsymbol{C}_h$=(1,1) and $\boldsymbol{C}_h$=(1,0), respectively. It is seen that the difference in Γ_G (predicted by the Griffith criterion) or Γ_{MD} (from direct MD simulations) along different orientations is rather small. However, a crack prefers to extend along the zigzag edge in graphene, which was due to the local strength-based failure rather than energy-based Griffith criterion [58].

3. Defects in graphene and mechanics of defected graphene

It is generally known that many properties of materials and structures are strongly affected or even determined by either intrinsic or extrinsic defects or their combination. This is more evident in the one-atom thick graphene and its derivatives like carbon nanotubes, fullerenes and so on. Indeed, it seems unavoidable for the presence of defects from geometrical necessity [115]. A typical fullerene, for example, is composed of twelve pentagons (see Fig. 3a). Understanding the mechanical properties of defects is a key challenge but aslo of particular importance for graphene. In this section, we summarize commonly seen defects in graphene and their mechanical description from up-to-date literature.

3.1 Typical defects

Defects in graphene may be categorized into three types if we differentiate how they are usually produced, i.e., thermal dynamically resulted, deformation introduced, and artificial ones. The thermally activated defects are generally of low energy level, like point vacancy and 5-7-7-5 rings, and 5-8-5 rings. Those defects are seen in graphene fabricated by different methods [116], and they also exist in other carbon allotropes like fullerene, carbon nanotube, and graphite. In particular, in grain boundaries of polycrystalline graphene, such defects are geometrical necessity to accommodate the incoherent lattice structure at lower energy. However, so far there are yet no reports regarding how frequently a typical thermal dynamic defect may appear. Identifying such defects like vacancy and non-hexagonal rings requires high-resolution tools, which renders a statistic analysis very time consuming and costly.

External deformation could also introduce such kind of defects; and it may even result in nanoscale cracks and nanoscale pores. Those mechanically triggered defects could be either transient or permanent in response to the removal of the deformation. Furthermore, to achieve a specific functionality, many groups have employed chemical strategies and high-energy bombing methods like irradiation to generate defects as well. We now introduce in detail those commonly seen defects and explain how they affect the nanomechanics of graphene.

The simplest example of topological disorder in graphene and other sp^2-hybridized carbon systems is the Stone-Thrower-Wales defect, usually called Stone-Wales, which results from rotating a C-C bond by 90◦ with regard to the midpoint of the bond—referred to as the SW transformation—so that four hexagons are turned into two pentagons and two heptagons [117, 118] (see Fig. 3b). Several derivatives had been identified, including the so-called inverse SW defect [119-122] and the di-vacancy defect [123], which is formed by the removal of two adjacent carbon atoms (Fig. 3c). It has been seen that grain boundaries are dominantly composed of pentagons-heptagon pairs to accommodate the lattice mismatch of pristine graphene flakes at different orientation, which is an important way to realize large-area but polycrystalline graphene, as seen in Fig. 3d. Reconstructed zigzag edges in GNR are also composed of pentagons-heptagon pairs, as proved by Jia et al. [80], Fig. 3e). More recently, Kim et al [124] demonstrated reversible and extended pentagon-heptagon (5-7) reconstruction at zigzag edges, and explored experimentally and theoretically the dynamics of the transitions between the edge configuration states.

By utilizing cutting-edge techniques, Warner et al. [125] determined the atomic structure, including the bond length and charge density variations of edge defects within extended arm chair defects in graphene, as well as bond elongation within a pair of 5-8-5 di-vacancies. Irradiation induced 5-8-5 defects [126] and grain boundaries formed by a group of 5-8-5 defects [127] had also been observed, as shown in Figs. 3f, g and h, respectively. There are also growing interests in making nanoscale defects in graphene for special applications, such as nanopores (Fig. 3i) in graphene-based membranes for molecular separation [128].

3.2 Pentagon-heptagon ring

Among all those different types of defects, the most-commonly seen pentagon-heptagon pairs deserve further consideration. Pentagon-heptagon pairs are analogous to dislocations in bulk crystalline materials, and are the most important defects in two-dimensional hexagonal lattice. From a geometrical perspective, a pentagon-heptagon pair resembles a disclination dipole [129-132], which consists of two disclinations of opposite signs. In the view of this, Wei et al. [26] constructed the stress field of a pentagon-heptagon pair by using the disclination dipole model. The stress components induced by a disclination dipole with a positive disclinations residing at (0, -*d*) and a negative one at (0, *d*) (see Fig. 4a) are given as:

$$\frac{\sigma_{xx}}{\sigma_0} = \frac{1}{2}\ln\frac{x^2+(y+d)^2}{x^2+(y-d)^2} + \frac{x^2}{x^2+(y-d)^2} - \frac{x^2}{x^2+(y+d)^2}, \tag{23a}$$

$$\frac{\sigma_{yy}}{\sigma_0} = \frac{1}{2}\ln\frac{x^2+(y+d)^2}{x^2+(y-d)^2} + \frac{x^2}{x^2+(y+d)^2} - \frac{x^2}{x^2+(y-d)^2}, \tag{23b}$$

$$\frac{\tau_{xy}}{\sigma_0} = \frac{x(y+d)}{x^2+(y+d)^2} - \frac{x(y-d)}{x^2+(y-d)^2}. \tag{23c}$$

The stress contours of σ_{xx}, σ_{yy}, and τ_{xy} predicted by the disclination dipole model, as seen in Figs. 4b to d, agree well with the large-scale MD simulations (Figs. 4e to g) produced by a pentagon-heptagon pair using a 1000nm×1000nm graphene sample in vacuum. Warner et al. [133] measured the strain fields of individual pentagon-heptagon pair, and showed how the defect deforms graphene by elongation and compression of C-C bonds, shear, and lattice rotations. The experimental result shown in Fig. 4h agrees well with the theoretical prediction. The stress fields described by eqn. (23) significantly differ from those of a dislocation within the core although they are similar for the region far away from the core. The accumulated effect by the local difference is important to understand grain boundary strength, as to be explained below.

3.3 Grain boundary

With the stress fields of individual pentagon-heptagon pair known, in particular the weak bond associated with the defect (see Figs. 4j and k), it is important to understand its influence on the strength of graphene. Accompanied with the development of synthesis techniques

capable of generating large area graphene, GBs were found to exist in most of the as-fabricated graphene [134-138], and those GBs are composed of pentagon-heptagon defects. Indeed, understanding how GBs primarily composed of pentagon-heptagon defects in graphene alter its physical properties is of both scientific and technological importance [24, 25, 138-143]. Recently, Biro and Lambin [144] reviewed the literatures on grain boundaries (GBs) in graphene, with a focus on the experimental findings on graphene grown by chemical vapor deposition (CVD) under a very wide range of experimental conditions (temperature, pressure hydrogen/hydrocarbon ratio, gas flow velocity, and substrates for growth). Here we summarize the theoretical advances on constructing the grain boundary and mechanical strength relationship.

3.3.1 The formation of two-dimensional grain boundaries

Geometrically, a general GB in three dimensional polycrystalline materials is characterized by five degrees of freedom, three from the relative rotation of adjacent grains and two due to the angular directions of the planar GB. For two dimensional polycrystalline graphene, only two rotational degrees of freedom are needed to define a general GB, the mis-orientation of the two grains (θ) and the rotation of the boundary line itself (ψ), as shown in Fig. 5a. For here and in what follows, we refer θ as grain mis-orientation and ψ as GB rotation. Figure 5b shows the atomic structures of GBs with constant θ but different ψ from 0^o to 27.5^o. The GB structures with constant ψ but θ varies 4.7^o to 27.5^o are shown in Fig. 5c [27]. It is interesting to note that the density of GB defects depends strongly on grain mis-orientation but is not sensitive to GB rotation.

The kinetic mechanisms leading to the type of grain boundaries have been broadly investigated. Cockayne et al. [142] presented a class of topological defects in graphene, composed of a rotating sequence of dislocations that close to themselves, forming grain boundary loops that either conserve the number of atoms in the hexagonal lattice or accommodate vacancy or interstitial reconstruction, while leaving no unsatisfied bonds. Such a grain boundary loop resembles “flower” pattern in scanning tunneling microscopy studies of epitaxial graphene grown on SiC(0001), as shown in Figs. 5d and e.

Theoretically, Seymour and Provatas [145] developed a new structural phase-field crystal (PFC) model which allows for stabilization of graphene, as well as the coexistence with a disordered phase. The model is adopted for efficient simulations for the nucleation and growth process of polycrystalline 2D materials, which shows the defect structures produced in CVD grown polycrystalline graphene. Ophus et al. [146] then characterized the structure of many different grain boundaries in single-layer graphene using HRTEM, and introduced a new algorithm for generating grain boundary structures for a class of hexagonal 2D materials. The authors found excellent agreement between the simulated and experimentally observed grain boundaries.

3.3.2 Strength of an individual GB

The formation of GBs would affect the strength of materials. The theoretical efforts studying the strength of GBs began with the exploration by Grantab et al. [25] who found that more GB defects could counter-intuitively give rise to higher strength in tilt GBs. A more comprehensive analysis by Wei et al. [26] demonstrated that GB strength can either increase or decrease with the tilt, and the behavior can be well explained by the stress fields introduced by pentagon-heptagon pairs as shown in section 3.2. It is not just the density of defects that affects the mechanical properties, but the detailed arrangement of defects is important. Well-stitched high angle grain boundaries in graphene would only slightly degrade its strength.

In the special case that grain boundaries are symmetrical tilt ones, the strengths of tilt GBs increase as the square of tilt angles if pentagon-heptagon defects are evenly spaced [26]. In that scenario, the residual stress S_{xx} in an infinitely long tilt GB with tilt angle θ (or equivalently GB mis-orientation) is given as

$$\frac{S_{xx}}{\sigma_0} = -\frac{2\pi^2 \Delta d}{3h_d^2}\frac{\theta^2}{\omega^2}, \qquad (24)$$

where Δ, d, h_d are geometrical parameters associated with the defects and their arrangement, ω is the rotational strength of the disclinations, and $\sigma_0 = E\omega/4\pi$ where E is the Young's modulus. The negative sign in eqn. (24) suggests that the residual stress

introduced by the neighbouring defects in the GB is compressive, which could compensate the exerted tensile stress and lead to high strength in the absence of interaction from other defects. Notably, the compressive stress at positive Δ (above the origin, on the side of the negative disclination) is proportional to θ^2. It is also important to know that ω is not $\pi/3$ from simple geometrical consideration, but a value depending on the type of grain boundaries. Table 2 lists the corresponding geometrical and material parameters for both armchair and zigzag tilt GBs [26]. An excellent agreement between theoretical analysis and molecular dynamics simulations was found, as shown in Fig. 5f.

In parallel to the theoretical analysis, two groups reported the strengths of individual grain boundaries experimentally. Lee et al. [8] combined the structural characterization by means of transmission electron microscopy with nano-indentation tests to study the mechanical properties of CVD-grown graphene films with different grain sizes. They found that the strength of graphene films is only slightly reduced despite the existence of grain boundaries. Indentation tests directly on grain boundaries confirmed that they are almost as strong as the pristine ones. Rasool et al. [9] measured the strengths of suspended bi-crystal graphene membranes with different GB mis-orientations, and revealed that grain boundaries with large mis-orientations in polycrystalline specimens have higher strengths than their low angle counterparts. These high angle grain boundaries even show strength comparable to that of single-crystal graphene. The higher strength in GBs of larger mis-orientations could be well explained by the larger compressive residual stress introduced by more neighboring pentagon-heptagon defects.

3.3.3 Strength of polycrystalline graphene

The understanding on the strength of individual GBs paves the road for understanding the strength of polycrystalline graphene containing abundant GBs, which is of significance in engineering practice. Suk et al. [147] studied the failure of CVD-grown polycrystalline graphene by nano-indentation test in a scanning electron microscope. Their measurement indicates that that graphene membranes without any grain boundaries had a failure strength of 45.4 ± 10.4 GPa, compared to 16.4 ± 5.1 GPa for those with grain boundaries. A large

variation in strength is seen. Shekhawat and Ritchie [148] investigated the statistical fluctuations in the toughness and the strength of polycrystalline graphene containing inherent nanoscale line and point defects—grain boundaries and grain-boundary triple junctions. They showed that the statistical variation in the toughness and the strength can be understood with ‘weakest-link' statistics, and elucidated the origins of the grain-size dependence of its strength and toughness. Such ‘weakest-link' statistics may be employed to explain the controversial observations from MD simulations. Sha et al. [149] showed that the breaking strength and average grain size in graphene follow an inverse pseudo Hall-Petch relation, in agreement with experimental measurements [9]. They also explained this inverse pseudo Hall-Petch relation by reasoning that the weakest-link determines the failure behavior of brittle materials. On the other hand, Song et al. [150] reported a Pseudo Hall–Petch strength reduction in polycrystalline graphene where samples of smaller grains exhibit higher strength. The observed crack localization and strength behavior were interpreted by a dislocation-piled-up model. The insensitiveness of flaws in nanocrystalline graphene could be originated from the statistical nature of defective GBs in competition with pre-existing flaws [151]. An interesting observation was made by Lin et al. [152] on the fracture behavior of the two-layer stacked graphene membranes using nano-indentation performed with an atomic force microscopy. The authors observed distinctly different fracture force distribution of stacked graphene from that of monolayer graphene: The stacked graphene membrane becomes less sensitive to the defects during nano-indentation, improving the overall performance of the graphene membranes.

It is worth noting that the original Hall-Petch relation is only strictly applicable to crystalline metals in which their strength is governed by the dislocation activities. It describes the strengthening mechanism resulted from grain boundaries by retarding dislocation motion; smaller grains in bulk polycrystalline materials imply more grain boundaries to serve as barriers to dislocation motion. Considering that no plastic deformation carrier is found in graphene at room temperature, applying the Hall-Petch relation in graphene might be a wrong shot. The ‘weakest-link’ statistics could be better suited to describe the grain size-dependent

strength in graphene. The strength-grain size relationship is all governed by the coherence of GBs and triple junctions in graphene.

3.4 Defect engineering

As every coin has two sides, defects in graphene could be engineered to realize particular structure configuration or certain exciting properties. Orlikowski [153] discussed the possibility of employing a combination of ad-dimers and strain to form nanotube-based quantum dots. By using the density functional theory calculations, Lust and Carr [154] reported a set of stable domain structures including blisters, ridges, ribbons, and meta-crystals. Through such a treatment, graphene with some particular chemical properties or ultra-fine pore could be also realized, while the latter could be utilized for specialized filtering and selective membranes for chemical and biological applications [155, 156].

For free-standing graphene, defects may introduce local compression given the graphene is flat. The compressive state is unstable, which leads to out-of-plane bulging from which the local high stress is relaxed by warping [10, 26, 157, 158]. Such mechanical deformation may be described by the generalized Föppl-Von Karman equation for a flexible solid membrane [70] and be utilized to design topological surfaces [70, 71, 159, 160], given that patterned defects could be synthesized.

Instead of changing graphene layers, Wang and Crespi [161] explored a way to engineer grain boundaries in two-dimensional crystals by controlling the substrate. They demonstrated that depositing graphene on a substrate of non-zero Gaussian curvature may facilitate the growth of *finite-length* grain boundaries that terminate abruptly within a mono-crystalline domain. By properly designing the substrate topography, these grain boundaries can be placed at desired locations and at specified misfit angles. New properties specific to certain grain boundary geometries, including magnetism and metallicity, can thus be engineered into 2D crystals through topographic design of their growth substrates.

3.5 Defect motion

The pentagon-heptagon defects – dislocations in the hexagonal 2-D lattice, has been investigated for motion possibility with the aim to making the strongest material to deform plastically.

The Stone-Wales defect has received a considerable amount of attention as it has the lowest formation energy among all intrinsic defects in the graphene system. As proposed by Yakobson [162], a pentagon-heptagon defect presumably plays an important role in plastic deformation of carbon nanotubes (CNTs) under tension by accommodating the strain, as detailed in Fig. 6a. Molecular dynamics simulations by Ding et al. [163] recaptured the deformation scenarios, as seen in Fig. 6b. Such simulations could also help to shed light on the diffusion, coalescence, and reconstruction of vacancy defects in graphene layers at elevated temperatures [164]. The suggested plastic deformation and kink formation in CNTs seems to agree well with the experimental observation [164]. Huang et al. reported that kink motion, in reminiscent of dislocation motion in crystalline materials, contributed to plastic deformation in all carbon nanotubes when being tensile loaded at high temperatures [165]. The deformation mechanism proposed by Yakobson [162] describes the main route of mechanical relaxation in a series of two-dimensional nano-crystals, suggesting a brittle cleavage at low temperature but plastic flow is likely at high temperatures or under electron radiation [166]. In both cases, deformation starts with diatomic rotation, which produces a dislocation dipole with the pentagon–heptagon cores. Under high stress, the defects depart from each other, leaving behind a permanent shearing [162, 167-169].

High resolution transmission electron microscopes (HRTEM) have been widely employed to exploit the motion of defects in graphene. Warner et al. [133] reported the stepwise dislocation movement along the zig-zag lattice direction mediated either by a single bond rotation or through the loss of two carbon atoms. The strain fields were determined, showing how yje dislocations deform graphene by elongation and compression of C-C bonds, shear, and lattice rotations. A cutting-edge aberration-corrected TEM study by Lehtinen et al. [168] demonstrated how the impinging energetic electrons stimulate atomic-scale

morphological changes in graphene. The full life cycle of transformations from the birth to annihilation, was seen *in situ*, and atom-by-atom (see Fig. 6d). Also with an aberration-corrected TEM, Kurasch et al. [169] used the energy of imaging electrons to stimulate individual bond rotations in the GB core region. They then observed *in situ*, atom-by-atom GB migration and its dependence on GB curvature. Scanning tunnelling microscopy (STM) was also broadly used to examine the growth of graphene on the Si-terminated facet of 6H-SiC (0001) [170]. The initial stages of ultrahigh vacuum graphitization resulted in the growth of individual graphene sheets on SiC terraces. The authors demonstrated that multilayer thickness resulted in high density of defects which located predominantly below the first layer of graphene.

The aforementioned research advances our understanding on the mobility of defects in graphene. The plastic deformations revealed so far, however, is contingent upon the assistance of the impinging energetic electrons or the help of high temperature. At room temperature, graphene sheets, either single layer or multiple layers, is brittle in nature. Even at high temperature or under irradiation, there is no literature reporting perceivable plasticity in graphene. While the mechanical performance of graphene at high temperature is very appealing, there seems to be a long way to go for achieving macroscopic plasticity in graphene.

4. Graphene on a substrate

Monolayer graphene exhibits rich morphology, including rippling in free-standing graphene introduced by stresses (see Fig. 7a) or thermal undulation. The mismatch of the coefficient of thermal expansion (CTE) between graphene and the substrate could induce strong compressive strain ($\varepsilon = \Delta T(\alpha_g - \alpha_{Cu})$) for a temperature drop ΔT in the graphene film (see Figs. 7b-i). Mechanically, two features are important to describe a graphene layer on a substrate, the adhesion energy and wrinkling. The wrinkling in graphene on a substrate is highly sensitive to the adhesion energy between graphene and the substrate [171, 172].

4.1 Adhesion

The adhesion between the graphene layers (in the case of multilayer graphene [18, 173]) or that between graphene and the substrate [13, 174-178] is critical for the transfer of the graphene layer as well. A number of experiments had been performed to obtain the adhesion energy of graphene on different substrates [13, 175-178]. There are two striking observations which are worth noting: (1) the values of graphene-substrate adhesion energy are greater than that of similar micromechanical systems, and one may attribute this characteristic to the low bending resistance of graphene, which promotes conforming contact of graphene with the substrates of arbitrary topography, and (2) the adhesion energy between single layer graphene and a substrate is significantly higher than that of a multi-layer graphene on the same substrate. For graphene of more than two layers, their adhesion energy on the same substrate remains nearly the same. For example, the adhesion energy of monolayer graphene and the silicon oxide was found to be $0.45\,Jm^{-2}$ and $0.31\,Jm^{-2}$ for samples containing two to five graphene layers [13, 171, 172]. The second observation reminds us to exercise caution when discussing the interaction of graphene with substrates.

4.2 Wrinkling

Once the strain energy resulted from thermal mismatch during cooling the graphene-substrate system is large enough to overcome their adhesion, the graphene layer buckles to form wrinkles, relaxes its in-plane compression at the expenses of interfacial energy due to delamination and bending energy in wrinkles. The wrinkles can form during both the growth and the transfer process which are very hard to release.

The wrinkling of graphene could be described using the continuum theory for thin elastic sheets. Cerda and Maha [179] deduced a general theory of wrinkling using elementary geometry and the physics of bending and stretching. Their main results include the scaling laws between the wavelength of the wrinkles λ with stiffness K due to an "elastic substrate" effect, with $\lambda \sim K^{-1/4}$, and the amplitude of the wrinkle $A \sim \lambda$. Given different crystallographic planes have distinct density of atomic packing and surface energy, there is a

strong dependence of wrinkling patterns on the substrate that graphene is grown on [180, 181].

For simplicity but without the loss of general physics, we may describe the out-of-plane displacement z of the wrinkles by a sinusoidal function,

$$z = Asin(2\pi y/\lambda), \quad (24),$$

where A is the amplitude and λ the wavelength. Wang and Devel [182] showed that the dependence of the ripple structure on the compressive edge strain ε should be governed by

$$\lambda^4 = \frac{4\pi^2 \nu L^2 t^2}{3(1-\nu^2)\varepsilon} \quad (25)$$

Bao et al. [183] reported the very first direct observation and controlled creation of one- and two-dimensional periodic ripples in suspended graphene sheets, using both spontaneously and thermally generated strains (see Fig. 7a). They demonstrated that the ripple orientation, wavelength and amplitude are tunable by controlling the boundary conditions and making use of the negative thermal expansion coefficient of graphene. Such manipulation of wrinkles may lead to advanced application of graphene-based nanoelectronics [184]. Under the influence of substrate, Tapaszto et al. [185] observed periodic rippling of nanometre-scale wavelength in the suspended graphene membranes under thermal strain using scanning tunnelling microscopy. The observed nano-rippling mode differs significantly from the predictions of the continuum mechanics model, which indicates the breakdown of applying the plate theory for graphene.

5. Perspectives

Regardless that the tremendous progress has been achieved on the deformation behaviour of graphene in response to mechanical or thermal undulation, there are still compelling needs to several key issues which cannot be satisfactorily addressed using the existing theories or computational tools. We comment below three mechanically-related issues which are of significance for the morphology manipulation of graphene in contact with substrates or under thermal undulation. Those issues call for further development in theory and computational tools for better predicting the mechanical behaviour of graphene.

5.1 Interlayer van der Waals interaction

The stacking of multiple layers of graphene forms graphite. The interlayer bond nature and its effective description are important for multilayer graphene as well as interactions of graphene with other structures. From a recent perspective by Geim and Grigorieva [186], research on graphene and other two-dimensional atomic crystals made layer by layer in a precisely chosen sequence, often referred to as 'van der Waals' heterostructures, may result in unusual properties and new phenomena. Such interaction, not surprisingly, would have a significant influence on the physical properties of those layered two-dimensional structures [187-189]. Van der Waals interaction could also be used for epitaxy, which is often limited by the need for lattice matching between the two material systems. This strict requirement is relaxed when epitaxy on layered two-dimensional (2D) materials, which is mediated by weak van der Waals interactions, and also allows facile layer release from 2D surfaces [190]. The mechanical behaviour of multiplayer graphene is fully determined by the interlayer van der Waals force. The interlayer shearing and rigidity affect the stiffness of a 'van der Waals' heterostructures [173]. The strength and fracture toughness also rely on how monolayers are bonded together.

While the in-plane deformation in graphene could be well captured by the all-electron density functional theory (DFT) calculations, popular density functionals for most first-principles based calculations are unable to describe correctly van der Waals interactions resulting from the dynamical correlations between fluctuating charge distributions [191]. In most atomistic simulations, practitioners chose the empirical Lennard-Jones (L-J) potentials to represent the interlayer interaction. Now the development is moving towards using the empirical correction for dispersion (van der Waals) effects (DFT-D method) by adding a semi-empirical dispersion potential to the conventional Kohn-Sham DFT energy to work around the limitation of DFT method and give better accuracy in contrast to the L-J approximation [191-193]. Different versions of the correction have then been developed. In a recent one by Grimme et al. [194, 195], more complicated, geometry-dependent dispersion coefficients and Becke-Jonson damping were taken into account. Cooper et al. [196-198] developed an exchange functional which is compatible with the nonlocal Rutgers-Chalmers

correlation functional (van der Waals density functional, vdW-DF). This functional, when employed with vdW-DF, demonstrates remarkable improvements on intermolecular separation distances while further improving the accuracy of vdW-DF interaction energies.

The DFT-D method and its derivatives have been broadly employed to capture the physics and mechanics of multilayer graphene [199-202], and the interaction of graphene with metal substrate [203]. It should be noted that the superlubricity in graphite [204] and weak shear strength [205] in graphene ought to be connected with the vdW characteristics between carbon layers. So far, even the DFT method and its derivatives are semi-empirical. They may work well in capturing one or several physical properties but are not justified to be accurate in general or other properties. A consensus on a reliable interaction formula to capture the vdW interaction in graphene is far from being reached. Another growing field of graphene is the interaction of graphene with other materials where an accurate atomic potential is desired for the commonly known fact that the accuracy of an atomistic simulation is by far no better than the potential one uses.

5.2 Limitation of thermal-mechanical coupling

At high temperatures, ripples are formed in free-standing graphene due to thermal fluctuations. The amplitude of ripples may be approximated from the free energy of the interface by a surface tension γ. If we consider the crumpled graphene surface, free energy in terms of surface tension times the surface area can be written as [206],

$$(\psi) = \gamma \int \sqrt{1 + \left|\vec{\nabla} h\right|^2}\, dx\, dy \approx \psi_0 + \frac{1}{2}\gamma \int \left|\vec{\nabla} h\right|^2 dx\, dy \qquad (26)$$

where h is the height of the graphene at each 2D position $\vec{r} = (x, y)$, the height-height correlation function may then be written as

$$\langle (h(\vec{r}) - h(\vec{0}))^2 \rangle = \frac{\int D(h(\vec{r}) \left|h(\vec{r}) - h(\vec{0})\right|^2 e^{-\psi/kT}}{\int D(h(\vec{r}) e^{-\psi/kT}} \qquad (27a)$$

The integral of the above equation leads to

$$\langle (h(\vec{r}) - h(\vec{0}))^2 \rangle \approx \frac{kT}{\pi\gamma} \ln(r/a), \text{ as } r \longrightarrow \infty \qquad (27b)$$

where *a* is a microscopic length. Equation (27) suggests that there is a divergent height-height correlation. The large r behavior is the signature of a rough surface at high temperature. In contrast, $\langle (h(\vec{r}) - h(\vec{0}))^2 \rangle \approx \text{const}$, as $r \longrightarrow \infty$ at low temperature, and we might expect a "smooth" interface. How such transition from smooth to rough surface influence the phononic thermal conductivity of a suspended 2-D material remains unclear. Rationales may help to shed light on the increasing in thermal conductivity of GNR with the sample size even when the size is beyond tens of microns.

5.3 Scale up

In its two-dimensional form, graphene is thought to be the strongest of all known materials. It is desirable to use such low-dimensional carbon structures as building blocks to realize three-dimensional (3-D) engineering materials and structures which may inherit their superb properties. There are many past and ongoing researches aiming to utilize the amazing mechanical properties of graphene and other carbon allotropes as strengthening agent in three dimensional structures [207, 208] or composites [209-213].

In reality, the scale-up leads to a substantial degradation of properties that we desire to retain. The realized mechanical and thermal properties of 3-D carbon materials, by staggering graphene sheets or vertically grown carbon nanotube arrays, are significantly lower than those of individual graphene sheets or individual CNTs [211]: the strongest graphene paper reported in the literature has a strength 2~3 orders of magnitude lower than that of graphene [210, 212]. The huge gap in the thermal and mechanical properties between the low-dimensional carbon allotropes and their 3-D derivatives originates from the dissimilar bonding characteristics between carbon atoms within graphene or CNTs and the architected 3-D engineering materials: The intra-structure bonding is covalent in nature, while van der Waals bonding dominates between different layers/tubes or with other materials [212]. Such heterogeneous bonding leads to property inheritance a mission impossible.

The interest in finding 3-D carbon structures has been lasting for decades. Recent success in the synthesis of carbon honeycomb (C-honeycomb) [214] shows a great potential in scaling

up the low-dimensional carbon allotropes to 3-D engineering materials and structures while retaining strong covalent bonding. Such a C-honeycomb structure may circumvent the change of bonding while using graphene as basic building blocks. Pang et al. [215] reported the atomistic structure of a stable 3-dimensional carbon honeycomb (C-honeycomb) structure. The authors demonstrated that a combination of sp^2 bonding in the wall and sp^3 bonding in the triple junction stabilize C-honeycomb. The detailed stable structures and their phonon dispersion are given in Fig. 8. Due to the low density in such stable 3-D architectured C-honeycomb with covalent bonding, its specific strength of C-honeycomb could be the best in structural carbon materials, and specific thermal conductivity is also much better than most metal and high thermal conductivity semiconductors, as clearly seen in Fig. 8g.

5.4 Summary and outlook

Since the successful peeling of graphene by Novoselov et al. [1], the mechanical properties of graphene have attracted great attentions from the research community. Examining the applicability of the classical mechanics theories to the materials with extreme aspect-ratio of large in-plane dimensions over one-atom thick limit, revealing new mechanical behaviours, and developing new theories to capture the nano-mechanics of graphene have been of the paramount interests. In this work, we review the current progress on the in-plane and out-of-plane mechanics of graphene. The structure-mechanical property relationship in graphene, in terms of its elasticity, strength, bending, with or without the defects, is presented. Although derived and validated at the macroscopic scale, several continuum theory formulae have been successfully applied to describe the elasticity of single layer graphene. It is also suggested that the currently developed theories and modelling tools for the deformation of graphene are probably applicable to other members in the growing family of two-dimensional materials. At the end, we also commented that several mechanics-related issues need to be addressed in the near future for better understanding the fascinating two-dimensional carbon allotrope.

The exploration on the extraordinary properties of graphene is strongly mechanically relevant: the original theory of structural instability in two-dimensional crystals is a pure mechanics concept; the very first way of obtaining single layer graphene is through

mechanical exfoliation by utilizing its ultra-small adhesion. We indeed would expect that mechanics may continue to play a pivotal role for the synthesis and the application of graphene. When graphene is functionalized as a critical component, intrinsic defects, pre-straining and morphology evolution due to lattice mismatch would all affect the final performance of the graphene-based system. For instance, wrinkles in graphene may lead to anisotropic electrical mobility [216], local charge accumulation [217], corrosion resistance degradation [218], and mechanical strength and thermal conductivity reduction [217, 219]. In contrast, we may also use graphene as a building block for further development of composite materials and heterostructures. In the latter circumstance, the properties of graphene including strength, fracture toughness, and adhesion at the microscopic level, will play important roles for the macroscopic properties of the hierarchically architectured materials. In addition, the rich morphology, abundant defects, as well as the defect-defect interaction, and morphology-defect coupling give rise to further challenge to obtain the structure-property relationship of graphene-based macroscopic materials. Given the attraction of graphene for nanomechanical systems [220] and composite materials [210, 212], many of the mechanical issues which are responsible for reliability and durability need to be addressed before the real world applications.

Funding

Y.W. acknowledges the support from National Natural Science Foundation of China (11425211). R.Y. acknowledges the support from the US National Science Foundation (1512776).

References

1. Novoselov, KS, Geim, AK, Morozov, SV et al. Electric field effect in atomically thin carbon films. Science 2004; 306: 666-9.
2. Geim, AK. Graphene: status and prospects. Science 2009; 324: 1530-4.
3. Mermin, ND. Crystalline order in two dimensions. Phys Rev 1968; 176: 250-4.
4. Landau, LD, Lifshitz, EM. Statistical Physics. Part I. Oxford: Pergamon Press, 1980.
5. Saito, R, Fujita, M, Dresselhaus, G et al. Physical Properties of Carbon Nanotubes. London: Imperial College London, 1998.
6. Hoffmann, R, Kabanov, AA, Golov, DM et al. Homo citans and carbon allotropes: for an ethics of citation. Angew Chem Int Ed 2016; 55: 10962-76.
7. Lee, C, Wei, X, Kysar, JW et al. Measurement of the elastic properties and intrinsic strength of monolayer graphene. Science 2008; 321: 385-8.
8. Lee, GH, Cooper, RC, An, SJ et al. High-strength chemical-vapor–deposited graphene and grain boundaries. Science 2013; 340: 1073-6.
9. Rasool, HI, Ophus, C, Klug, WS et al. Measurement of the intrinsic strength of crystalline and polycrystalline graphene. Nat Comm 2013; 4: 2811.
10. Yakobson, BI, Brabec, CJ, Bernholc, J. Nanomechanics of carbon tubes: instabilities beyond linear response. Phys Rev Lett 1996; 76: 2511-4.
11. Fasolino, A, Los, JH, Katsnelson, MI. Intrinsic ripples in graphene. Nat Mater 2007; 6: 858.
12. Liu, Y, Yakobson, BI. Cones, pringles, and grain boundary landscapes in graphene topology. Nano Lett 2010; 10: 2178-83.
13. Koenig, SP, Boddeti, NG, Dunn, ML et al. Ultrastrong adhesion of graphene membranes. Nat Nanotechnol 2011; 6: 543-6.
14. Gao, Y, Liu, LQ, Zu, SZ et al. The effect of interlayer adhesion on the mechanical behaviors of macroscopic graphene oxide papers. ACS nano 2011; 5: 2134-41.
15. Sen, D, Novoselov, KS, Reis, PM et al. Tearing graphene sheets from adhesive substrates produces tapered nanoribbons. Small 2010; 6: 1108-16.
16. Shi, X, Yin, Q, Wei, Y. A theoretical analysis of the surface dependent binding, peeling and folding of graphene on single crystal copper. Carbon 2012; 50: 3055-63.
17. Na, SR, Suk, JW, Tao, L et al. Selective mechanical transfer of graphene from seed copper foil using rate effects. ACS nano 2015; 9: 1325-35.
18. Filleter, T, McChesney, JL, Bostwick, A et al. Friction and dissipation in epitaxial graphene films. Phys Rev Lett 2009; 102: 086102.
19. Lee, C, Li, Q, Kalb, W et al. Frictional characteristics of atomically thin sheets. Science 2010; 328: 76-80.
20. Choi, JS, Kim, JS, Byun, IS et al. Friction anisotropy–driven domain imaging on exfoliated monolayer graphene. Science 2011; 333: 607-10.
21. Guo, Y, Guo, W, Chen, C. Modifying atomic-scale friction between two graphene sheets: A molecular-force-field study. Phys Rev B 2007; 76: 155429.
22. Zhang, Z, Kutana, A, Yakobson, BI. Edge reconstruction-mediated graphene fracture. Nanoscale 2015; 7: 2716-22.
23. An, J, Voelkl, E, Suk, JW et al. Domain (grain) boundaries and evidence of “twinlike” structures in chemically vapor deposited grown graphene. ACS nano 2011; 5: 2433-39.

24. Huang, PY, Ruiz-Vargas, CS, van der Zande, AM et al. Grains and grain boundaries in single-layer graphene atomic patchwork quilts. Nat 2011; 469: 389-92.
25. Grantab, R, Shenoy, VB, Ruoff, RS. Anomalous strength characteristics of tilt grain boundaries in graphene. Science 2010; 330: 946-8.
26. Wei, Y, Wu, J, Yin, H et al. The nature of strength enhancement and weakening by pentagon–heptagon defects in graphene. Nat Mater 2012; 11: 759-63.
27. Wu, J, Wei, Y. Grain misorientation and grain-boundary rotation dependent mechanical properties in polycrystalline graphene. J Mech Phys Solids 2013; 61: 1421-32.
28. Teng,L, Li, X, Gao, H. Fracture of graphene: a review. Int. J. Fracture 2015; 196: 1-31.
29. Cao, C, Sun, Y, Filleter, T. Characterizing mechanical behavior of atomically thin films: A review. J. Mater Res 2014; 29: 338-47.
30. Ivanovskii, AL. Graphene-based and graphene-like materials. Russ Chem Rev 2012; 81: 571-605.
31. Penkov, O, Kim, HJ, Kim, HJ et al. Tribology of graphene: a review. Int J Pr Eng Man 2014; 15: 577-85.
32. Akinwande, D, Brennan, CJ, Bunch, JS et al. A review on mechanics and mechanical properties of 2D materials—Graphene and beyond. Extreme Mechanics Letters 2017; 13: 42-77.
33. Penev, ES, Artyukhov, VI, Ding, F et al. Unfolding the fullerene: nanotubes, graphene and poly-elemental varieties by simulations. Adv Mater 2012; 24: 4956-76.
34. Neto, AC, Guinea, F, Peres, NM et al. The electronic properties of graphene. Rev Mod Phys 2009; 81: 109.
35. Ando, T. The electronic properties of graphene and carbon nanotubes. NPG asia materials 2009; 1: 17-21.
36. Katsnelson, MI. Graphene: carbon in two dimensions. Materials Today 2007; 10: 20-7.
37. Neto, AHC. The electronic properties of graphene. Vacuum 2007; 244: 4106-11.
38. Allen, MJ, Tung, VC, Kaner, RB. Honeycomb carbon: a review of graphene. Chem. Rev. 2010; 110: 132-45.
39. Liu, Z. Graphene: From basic science to useful technology. Natl Sci Rev 2015; 2: 16.
40. Wu, ZS, Feng, X, Cheng, HM. Recent advances in graphene-based planar micro-supercapacitors for on-chip energy storage. Natl Sci Rev 2014; 1: 277-92.
41. Gu, X, Wei, Y, Yin, X et al. Phononic thermal properties of two-dimensional materials. arXiv preprint 2017; arXiv:1705.06156.
42. Mermin, ND, Wagner, H. Absence of Ferromagnetism or Antiferromagnetism in One- or Two-Dimensional Isotropic Heisenberg Models, Phys Rev Lett 1966; 17: 1133–6.
43. Peierls RE, Helv Phys Acta 1923; 7: 81
44. Landau, LD. Zur Theorie der phasenumwandlungen II. Phys Z Sowjetunion 1937; 11: 26-35.
45. Alder BJ, Wainwright TE. Phase Transition in Elastic Disks. Phys Rev 1962; 127: 359–61.
46. Shenderova, OB, Zhirnov, VV, Brenner, DW. Carbon Nanostructures. Critical Reviews in Solid State and Materials Sciences 2002; 27: 227–356.
47. Kumar, S, Parks, DM. A comprehensive lattice-stability limit surface for graphene. J Mech Phys Solids 2016; 86: 19-41.
48. Geim AK, Novoselov, AK. The rise of graphene. Nat Mater 2007; 6:183–91.
49. Singh V, Joung D, Zhai L et al. Graphene based materials: past, present and future. Prog Mater Sci 2011; 56: 1178–271.
50. Pereira, VM, Castro Neto, AH, Peres, NMR. A tight-binding approach to uniaxial strain in

graphene Phys. Rev. B 2009; 80:045401.
51. Gibson, LJ, Ashby, MF. Cellular Solids, structure and properties, 2nd Ed. P101, Cambridge Press, 1997.
52. Liu, F, Ming, P, Li, J. Ab initio calculation of ideal strength and phonon instability of graphene under tension. Phys Rev B 2007; 76: 064120.
53. Van Lier, G, Van Alsenoy, C, Van Doren, V et al. Ab initio study of the elastic properties of single-walled carbon nanotubes and graphene. Chem Phys Lett 2000; 326: 181-5.
54. Zakharchenko, KV, Katsnelson, MI, Fasolino, A. Finite Temperature Lattice Properties of Graphene beyond the Quasiharmonic Approximation. Phys Rev Lett 2009; 102: 046808.
55. Bhatia, NM, Nachbar, W. Finite indentation of an elastic membrane by a spherical indenter. Int J Nonlinear Mech 1968; 3: 307–24.
56. Brugger, K. Determination of 3rd-order elastic coefficients in crystals. J Appl Phys 1965; 36: 768–73.
57. Cadelano, E, Palla, PL, Giordano, S et al. Nonlinear elasticity of monolayer graphene. Phys Rev Lett 2009; 102: 235502.
58. Yin, H, Qi, HJ, Fan, F et al. Griffith criterion for brittle fracture in graphene. Nano Lett 2015; 15: 1918-24.
59. Wei, Y, Wang, B, Wu, J et al. Bending rigidity and Gaussian bending stiffness of single-layered graphene. Nano Lett 2012; 13: 26-30.
60. Sanchez-Portal, D, Artacho, E, Soler, JM et al. Ab initio structural, elastic, and vibrational properties of carbon nanotubes. Phys Rev B 1999; 59: 12678.
61. Arroyo, M, Belytschko, T. Finite crystal elasticity of carbon nanotubes based on the exponential Cauchy-Born rule. Phys Rev B 2004; 69: 115415.
62. Koskinen, P, Kit, OO. Approximate modeling of spherical membranes. Phys Rev B 2010; 82: 235420.
63. Nicklow, R, Wakabayashi, N, Smith, HG. Lattice dynamics of pyrolytic graphite. Phys Rev B 1972; 5: 4951.
64. Helfrich, W. Elastic properties of lipid bilayers: Theory and possible experiments. Zeitschrift fur Naturforschung C 1973; 28: 693-703.
65. Lipowsky, R. The conformation of membranes. Nat 1991; 349: 475–81.
66. Timoshenko, S, Woinowsky-Krieger, S. Theory of Plates and Shells. 2nd ed. McGRAW-HILL Book Company, 1959.
67. Yu, L, Ru, CQ. Non-classical mechanical behavior of an elastic membrane with an independent Gaussian bending rigidity. Math Mech Solids 2015; 22: 491-501.
68. Davini, C, Favata, A, Paroni, R. The bending behavior of graphene: a continuum model inferred from molecular dynamics. J Mech Phys Solids 2017; 104: 96-114.
69. Ahmadpoor, F, Wang, P, Huang, R et al. Thermal fluctuations and effective bending stiffness of elastic thin sheets and graphene: a nonlinear analysis. J Mech Phys Solids 2017; 107: 294-319.
70. Zhang, T, Li, X, Gao, H. Defects controlled wrinkling and topological design in graphene. J Mech Phys Solids 2014, 67: 2-13.
71. Zhang, T, Li, X, Gao, H. Designing graphene structures with controlled distributions of topological defects: A case study of toughness enhancement in graphene ruga. Extreme Mechanics Letters 2014; 1: 3-8.
72. Boddeti, NG, Liu, X, Long, R et al. Graphene blisters with switchable shapes controlled by

pressure and adhesion. Nano Lett 2013; 13: 6216-21.
73. Girit, CO, Meyer, JC, Erni, R et al. Graphene at the edge: Stability and dynamics. Science 2009; 323: 1705–08.
74. Voznyy, O, Güçlü, AD, Potasz, P et al. Effect of edge reconstruction and passivation on zero-energy states and magnetism in triangular graphene quantum dots with zigzag edges. Phys Rev B Cond Matter 2012; 83: 5919-26.
75. Zhang Z, Kutana A, Yakobson BI. Edge reconstruction-mediated graphene fracture. Nanoscale 2015; 7: 2716.
76. Berger, C, Song, Z, Li, X et al. Electronic confinement and coherence in patterned epitaxial graphene. Science 2006; 312:, 1191-6.
77. Ozyilmaz, B, Jarillo-Herrero, P, Efetov, D et al. Electronic transport and quantum hall effect in bipolar graphene p− n− p junctions. Phys Rev Lett 2007; 99: 166804.
78. Li, X, Wang, X, Zhang, L et al. Chemically Derived, Ultrasmooth Graphene Nanoribbon Semiconductors. Science 2008; 319: 1229-32.
79. Campos-delgado J, Romoherrera JM, Jia, X et al. Bulk Production of a New Form of sp2 Carbon: Crystalline Graphene Nanoribbons. Nano Lett 2008; 8: 2773–8
80. Jia X, Dresselhaus MS. Controlled Formation of Sharp Zigzag and Armchair Edges in Graphitic Nanoribbons. Science 2009; 323: 1701-5.
81. Acik, M, Chabal, YJ. Nature of graphene edges: a review. Japanese J Appl Phys 2011; 50: 070101.
82. Nakada, K, Fujita, M, Dresselhaus, G et al. Edge state in graphene ribbons: Nanometer size effect and edge shape dependence. Phys Rev B 1996; 54: 17954.
83. Son, YW, Cohen, ML, Louie, SG. Energy gaps in graphene nanoribbons. Phys Rev Lett 2006; 97: 216803.
84. Cançado, LG, Pimenta, MA, Neves, BRA et al. Anisotropy of the Raman Spectra of Nanographite Ribbons. Phys Rev Lett 2004; 93: 047403
85. Jorio, A, Dresselhaus, G, Dresselhaus, MS. Carbon Nanotubes: Advanced Topics in the Synthesis, Structure, Properties and Applications. Berlin: Springer-Verlag, 2008.
86. Panchakarla, LS, Govindaraj, A, Rao, CNR. Nitrogen- and Boron-Doped Double-Walled Carbon Nanotubes. ACS Nano 2007; 1: 494-500
87. Hu, J, Ruan, X, Chen, YP. Thermal conductivity and thermal rectification in graphene nanoribbons: a molecular dynamics study. Nano Lett 2010; 9: 2730-5.
88. Ritter, KA, Lyding, JW. The influence of edge structure on the electronic properties of graphene quantum dots and nanoribbons. Nat Mater 2009; 8: 235-42.
89. Zhang, X, Xin, J, Ding, F. The edges of graphene. Nanoscale 2013; 5: 2556-69.
90. Kim, K, Lee, Z, Malone, BD et al. Multiply folded graphene. Phys Rev B 2011; 83: 245433.
91. Shenoy, VB, Reddy, CD, Ramasubramaniam, A et al. Edge-stress-induced warping of graphene sheets and nanoribbons, Phys Rev Lett 2008; 101: 245501.
92. Reddy, CD, Ramasubramaniam, A, Shenoy, VB et al. Edge elastic properties of defect-free single-layer graphene sheets. Appli Phys Lett 2009; 94: 101904.
93. Zhao, H, Min, K, Aluru, NR. Size and Chirality Dependent Elastic Properties of Graphene Nanoribbons under Uniaxial Tension. Nano Lett 2009; 9: 3012-5
94. Wang, H, Upmanyu, M. Rippling instabilities in suspended nanoribbons. Phys Rev B 2012; 86: 205411.
95. Lu, Q, Huang, R. Excess energy and deformation along free edges of graphene nanoribbons. Phys

Rev B 2010; 81: 155410.
96. Gan, CK, Srolovitz, DJ. First-principles study of graphene edge properties and flake shapes. Phys Rev B 2010; 81: 125445.
97. Cranford S, Buehler MJ. Twisted and coiled ultralong multilayer graphene ribbons. Model SimuL Mater Sci Eng 2011; 19: 054003.
98. Landau LD, Lifshitz EM. Theory of elasticity. Oxford: Pergamon Press, 1986.
99. Stuart, SJ, Tutei, AB, Harrison, JA. A reactive potential for hydrocarbons with intermolecular interactions, J Chem Phys 2000; 112: 6472-86.
100. Plimpton, SJ. Fast Parallel Algorithms for Short-Range Molecular Dynamics, J Comp Phys 1995; 117: 1-19
101. Garcia-Sanchez D, van der Zande AM, Paulo AS, et al. Imaging mechanical vibrations in suspended graphene sheets. Nano lett 2008; 8: 1399-403.
102. Lu, Q, Huang, R. Excess energy and deformation along free edges of graphene nanoribbons. Phys Rev B 2010; 81: 155410 .
103. Dewapriya, MAN., Phani, AS, Rajapakse, RKND. Influence of temperature and free edges on the mechanical properties of graphene. Model Simul Mater Sci Eng 2013; 21: 2848-55.
104. Li, F, Cheng, HM, Bai, S et al. Tensile strength of single-walled carbon nanotubes directly measured from their macroscopic ropes. Appl Phys Lett 2000; 77: 3161-3.
105. Demczyk, BG, Wang, YM, Cumings, J et al. Direct mechanical measurement of the tensile strength and elastic modulus of multiwalled carbon nanotubes. Mater Sci Eng A 2002; 334: 173-8.
106. Kumar, S, Parks, DM. Strain shielding from mechanically activated covalent bond formation during nanoindentation of graphene delays the onset of failure. Nano Lett 2015; 15: 1503-10.
107. Wang, B, Wu, J, Gu, X et al. Stable planar single-layer hexagonal silicene under tensile strain and its anomalous Poisson's ratio. Appl Phys Lett 2014; 104: 081902.
108. Kim, K, Artyukhov, VI, Regan, W et al. Ripping graphene: preferred directions. Nano Lett 2012; 12:, 293-7.
109. Griffith, AA. The phenomena of rupture and flow in solids, Phil. Trans Roy Soc 1921; 221: 163–98.
110. Bazant, ZP, Planas, J. Fracture and size effect: in concrete and other quasi brittle materials Taylor & Francis, CRC Press, Boca Raton, FL, 1998.
111. Zhang, P, Ma, L, Fan, F et al. Fracture toughness of graphene. Nat Comm 2014; 5: 3782.
112. Hwangbo, Y, Lee, CK, Kim, SM et al. Fracture characteristics of monolayer cvd-graphene. Sci Rep 2014; 4: 4439.
113. Wei, X, Xiao, S, Li, F et al. Comparative fracture toughness of multilayer graphenes and boronitrenes. Nano Lett 2015; 15: 689-94.
114. Jhon, YI, Jhon, YM, Yeom, GY, Jhon, MS. Orientation dependence of the fracture behavior of graphene. Carbon 2014; 72: 619-28.
115. Araujo, PT, Terrones, M, Dresselhaus, MS. Defects and impurities in graphene-like materials. Materials Today 2012; 15: 98-109.
116. Eletskii, AV, Iskandarova, IM, Knizhnik, AA et al. Graphene: fabrication methods and thermophysical properties. Physics-Uspekhi 2011; 54: 227-58.
117. Thrower, DA. In: Chemistry and physics of carbon, vol. 5, ed. Walker, Jr. P.L., Marcel Dekker, New York (1969).

118. Stone, AJ, Wales, DJ. Theoretical Studies of Icosahedral C60 and Some Related Species. Chem Phys Lett 1986; 128: 501–3.
119. Terrones, H, Terrones, M, Hernández, E et al. New metallic allotropes of planar and tubular carbon. Phys Rev Lett 2000; 84: 1716.
120. Lusk, MT, Carr, LD. Nanoengineering defect structures on graphene. Phys Rev Lett 2008; 100: 175503.
121. Li, L, Reich, S, Robertson, J. Defect energies of graphite: Density-functional calculations. Phys Rev B 2005; 72: 184109.
122. Orlikowski, D, Nardelli, MB, Bernholc, J et al. Ad-dimers on strained carbon nanotubes: A new route for quantum dot formation. Phys Rev Lett 1999; 83: 4132.
123. Hashimoto, A, Suenaga, K, Gloter, A et al. Direct evidence for atomic defects in graphene layers. Nat 2004; 430: 870-3.
124. Kim, K, Coh, S, Kisielowski, C et al. Atomically perfect torn graphene edges and their reversible reconstruction. Nat Comm. 2013; 4: 2723.
125. Warner, JH, Lee, GD, He, K et al. Bond length and charge density variations within extended arm chair defects in graphene. Acs Nano 2013; 7: 9860-6.
126. Kotakoski, J, Krasheninnikov, AV, Kaiser, U et al. From point defects in graphene to two-dimensional amorphous carbon. Phys Rev Lett 2011; 106: 105505.
127. Lahiri, J, Lin, Y, Bozkurt, P et al. An extended defect in graphene as a metallic wire. Nat Nanotechnol 2010; 5: 326-9.
128. Jiang, DE, Cooper, VR, Dai, S. Porous graphene as the ultimate membrane for gas separation. Nano Lett 2009; 9: 4019-24.
129. Li, JCM. Disclination model of high angle grain boundaries. Surf Sci 1972; 31, 12-26.
130. Shih, KK, Li, JCM. Energy of grain boundaries between cuspmisorientations. Surf Sci 1975; 50: 109-24.
131. Kleman, M, Friedel, J. Disclinations, dislocations, and continuous defects: A reappraisal. Rev Mod Phys 2008; 80: 61-115.
132. Romanov, AE, Kolesnikova, AL. Application of disclination concept to solid structures. Prog Mater Sci 2009; 54, 740-69.
133. Warner, JH, Margine, ER, Mukai, M et al. Dislocation-driven deformations in graphene. Science 2012; 337: 209-12.
134. Li, X, Cai, W, An, J et al. Large-area synthesis of high-quality and uniform graphene films on copper foils. Science 2009; 324: 1312-4.
135. Kim, KS, Zhao, Y., Jang, H et al. Large-scale pattern growth of graphene films for stretchable transparent electrodes. Nat 2009; 457: 706-10.
136. Reina, A, Jia, X, Ho, J et al. Large Area, few-layer graphene films on arbitrary substrates by chemical vapor deposition. Nano Lett 2008; 9: 30-5.
137. Park, S, Ruoff, RS. Chemical methods for the production of graphenes. Nat Nanotechnol 2009; 4, 217-24.
138. Zhao, L., Rim, K.T., Zhou, H et al. The atomic-scale growth of large-area monolayer graphene on single-crystal copper substrates. arXiv preprint arXiv 2010; 1008.3542.
139. Yu, Q, Jauregui, LA, Wu, W et al. Control and characterization of individual grains and grain boundaries in graphene grown by chemical vapour deposition. Nat Mater 2011; 10: 443-9.
140. Yazyev, OV Louie, SG. Electronic transport in polycrystalline graphene. Nat Mater 2010; 9: 806-9.

141. Malola, S, Häkkinen, H, Koskinen, P. Structural, chemical, and dynamical trends in graphene grain boundaries. Phys Rev B 2010; 81: 165447.
142. Cockayne, E, Rutter, GM, Guisinger, NP et al. Grain boundary loops in graphene. Phys Rev B 2011; 83: 195425.
143. Kim, P. Graphene: Across the border. Nat Mater 2010; 9: 792-3.
144. Biró, LP, Lambin, P. Grain boundaries in graphene grown by chemical vapor deposition. New J Phys 2013; 15: 035024.
145. Seymour, M, Provatas, N. Structural phase field crystal approach for modeling graphene and other two-dimensional structures. Phys Rev B 2016; 93: 035447.
146. Ophus, C, Shekhawat, A, Rasool, HI et al. Large-scale experimental and theoretical study of graphene grain boundary structures. Phys Rev B 2015; 92: 205402.
147. Suk, JW, Mancevski, V, Hao, Y et al. Fracture of polycrystalline graphene membranes by in situ nanoindentation in a scanning electron microscope. Physica Status Solidi 2015; 9: 564-9.
148. Shekhawat, A, Ritchie, RO. Toughness and strength of nanocrystalline graphene. Nat Comm 2016; 7: 10546.
149. Sha, ZD, Quek, SS, Pei, QX et al. Inverse pseudo hall-petch relation in polycrystalline graphene. Sci Rep 2014; 4: 5991.
150. Song, Z, Artyukhov, VI, Yakobson, BI et al. Pseudo hall–petch strength reduction in polycrystalline graphene. Nano Lett 2013; 13: 1829.
151. Zhang, T, Li, X, Kadkhodaei, S et al. Flaw insensitive fracture in nanocrystalline graphene Nano Lett. 2012; 12: 4605-10.
152. Lin, QY, Zeng, YH, Liu, D et al. Step-by-step fracture of two-layer stacked graphene membranes. Acs Nano 2014; 8: 10246-51.
153. Orlikowski, D, Nardelli, MB, Bernholc, J et al. Ad-dimers on strained carbon nanotubes: A new route for quantum dot formation?. Phys Rev Lett 1999; 83: 4132.
154. Lusk, MT, Carr, LD. Nanoengineering defect structures on graphene. Phys Rev Lett 2008; 100: 175503.
155. O'Hern, SC, Boutilier, MS, Idrobo, JC et al. Selective ionic transport through tunable subnanometer pores in single-layer graphene membranes. Nano lett. 2014; 14: 1234-41.
156. Radha, B, Esfandiar, A, Wang, FC et al. Molecular transport through capillaries made with atomic-scale precision. Nature, 2016; 538: 222-25.
157. Liu, Y, Yakobson, BI. Cones, pringles, and grain boundary landscapes in graphene topology. Nano Lett 2010; 10: 2178-83.
158. Bhowmick, S, Waghmare, UV. Anisotropy of the Stone-Wales defect and warping of graphene nanoribbons: A first-principles analysis. Phys Rev B 2010; 81: 155416.
159. Carpio, A, and Bonilla, LL. Periodized discrete elasticity models for defects in graphene, Phys Rev B 2008; 78: 085406.
160. Wales, DJ. Chemistry, geometry, and defects in two dimensions. Acs Nano 2014; 8: 1081.
161. Wang, Y, Crespi, VH. Theory of finite-length grain boundaries of controlled misfit angle in two-dimensional materials. Nano Lett 2017; 17: 5297-5303.
162. Yakobson, BI. Mechanical relaxation and "intramolecular plasticity" in carbon nanotubes. Appl Phys Lett 1998; 72: 918-920.
163. Ding, F, Jiao, K, Wu, M et al. Pseudoclimb and dislocation dynamics in superplastic nanotubes. Phys Rev Lett 2007; 98: 075503.

164. Lee et al. Diffusion, Coalescence, and Reconstruction of Vacancy Defects in Graphene Layers. Phys Rev Lett 2005; 95: 205501.
165. Huang, JY, Chen, S, Ren, ZF. Kink formation and motion in carbon nanotubes at high temperatures. Phys Rev Lett 2006; 97: 075501.
166. Kotakoski, J, Meyer, JC, Kurasch, S et al. Stone-Wales-type transformations in carbon nanostructures driven by electron irradiation. Phys Rev B 2011; 83: 245420.
167. Chen, S, Ertekin, E, Chrzan, DC. Plasticity in carbon nanotubes: Cooperative conservative dislocation motion. Phys Rev B 2010; 81: 155417.
168. Lehtinen, O, Kurasch, S, Krasheninnikov, AV et al. Atomic scale study of the life cycle of a dislocation in graphene from birth to annihilation. Nat Comm 2013; 4: 2098.
169. Kurasch, S, Kotakoski, J, Lehtinen, O et al. Atom-by-atom observation of grain boundary migration in graphene. Nano Lett 2012; 12: 3168-3173.
170. Guisinger, NP, Rutter, GM, Crain, JN et al. Atomic-scale investigation of graphene formation on 6H-SiC(0001). J Vac Sci Technol A 2008; 26: 932-7.
171. Bunch, JS, Dunn, ML Adhesion mechanics of graphene membranes. Solid State Commun 2012; 152: 1359-64.
172. Koenig, SP. Graphene Membranes: Mechanics, Adhesion, and Gas Separations. Ph.D. Thesis. The University of Colorado at Boulder 2013.
173. Peng SY, Wei YJ. On the influence of interfacial properties to the bending rigidity of layered structures, J Mech Phys Solids 2016; 92, 278-96.
174. Lu, Z, Dunn, ML van der Waals adhesion of graphene membranes. Journal of Applied Physics 2010; 107: 044301.
175. Scharfenberg, S, Rocklin, DZ, Chialvo, C et al. Probing the mechanical properties of graphene using a corrugated elastic substrate. Applied Physics Letters 2011; 98: 091908.
176. Zong, Z, Chen, CL, Dokmeci, MR et al. Direct measurement of graphene adhesion on silicon surface by intercalation of nanoparticles 2010; 107: 026104
177. Yoon, T, Shin, WC, Kim, TY et al. Direct measurement of adhesion energy of monolayer graphene as-grown on copper and its application to renewable transfer process. Nano letters 2012; 12: 1448-52.
178. Scharfenberg, S, Mansukhani, N, Chialvo, C et al. Observation of a snap-through instability in graphene. Applied Physics Letters 2012; 100: 021910.
179. Cerda, E, Mahadevan, L. Geometry and physics of wrinkling. Phys Rev Lett 2003; 90: 074302.
180. Liu X, Wang F, Wu H. Anisotropic growth of buckling-driven wrinkles in graphene monolayer. Nanotech 2015; 26: 065701.
181. Deng, B, Pang, Z, Chen, S et al. Wrinkle-Free Single-Crystal Graphene Wafer Grown on Strain-Engineered Substrates. ACS nano 2017; 11: 12337-45.
182. Wang, Z, Devel, M. Periodic ripples in suspended graphene. Phys Rev B 2011; 83: 125422.
183. Bao, W, Miao, F, Chen, Z et al. Controlled ripple texturing of suspended graphene and ultrathin graphite membranes. Nat Nanotech 2009; 4: 562-6.
184. Qin, Z, Taylor, M, Hwang, M et al. Effect of wrinkles on the surface area of graphene: toward the design of nanoelectronics. Nano Lett 2014; 14: 6520-6525.
185. Tapasztó, L, Dumitrică, T, Kim, SJ et al. Breakdown of continuum mechanics for nanometre-wavelength rippling of graphene. Nat Phys 2013; 8: 739-742.
186. Geim, AK, Grigorieva, IV. Van der Waals Heterostructures. Nat 2013; 499: 419-25.

187. Ruoff, RS, Tersoff, J, Lorents, DC et al. Radial deformation of carbon nanotubes by van der waals forces. Nat 1993; 364: 514-6.
188. Dappe, YJ, Basanta, MA, Flores, F et al. Weak chemical interaction and van der Waals forces between graphene layers: A combined density functional and intermolecular perturbation theory approach. Phys Rev B 2006; 74: 205434.
189. Balandin, AA. Phonon engineering in graphene and van der waals materials. MRS Bulletin 2014; 39: 817-23.
190. Kim, Y, Cruz, SS, Lee, K et al. Remote epitaxy through graphene enables two-dimensional material-based layer transfer. Nat 2017, 544: 340-3.
191. Dion, M, Rydberg, H, Schröder, E et al. Van der Waals density functional for general geometries. Phys Rev Lett 2004; 92: 246401.
192. Harl, J, Kresse, G. Accurate bulk properties from approximate many-body techniques. Phys Rev Lett 2009; 103: 056401.
193. Harl, J, Schimka, L, Kresse, G. Assessing the quality of the random phase approximation for lattice constants and atomization energies of solids. Phys Rev B 2010; 81: 115126.
194. Grimme, S, Antony, J, Ehrlich, S et al. A consistent and accurate ab initio parametrization of density functional dispersion correction (DFT-D) for the 94 elements H-Pu. J Chem Phys 2010; 132: 154104.
195. Grimme, S, Ehrlich, S, Goerigk, L. Effect of the damping function in dispersion corrected density functional theory. J Comp Chem 2011; 32: 1456-65.
196. Cooper, VR. Van der Waals density functional: An appropriate exchange functional. Phys Rev B 2010; 81: 161104(R).
197. Lee, K, Murray, ÉD, Kong, L et al. Higher-accuracy van der Waals density functional. Phys Rev B 2010; 82: 081101.
198. Berland, K, Hyldgaard, P. Exchange functional that tests the robustness of the plasmon description of the van der Waals density functional. Phys Rev B 2014; 89: 035412.
199. Lebedeva, IV, Knizhnik, AA, Popov, AM et al. Interlayer interaction and relative vibrations of bilayer graphene. Physical Chemistry Chemical Physics 2011; 13: 5687-95.
200. Ruiz, L, Xia, W, Meng, Z, Keten, S. A coarse-grained model for the mechanical behavior of multi-layer graphene. Carbon 2014; 82: 103-15.
201. Zhang, YY, Wang, CM, Cheng, Y et al. Mechanical properties of bilayer graphene sheets coupled by sp 3, bonding. Carbon 2011; 49: 4511–7.
202. Dappe, YJ, Bolcatto, PG, Ortega, J et al. Dynamical screening of the van der waals interaction between graphene layers. J Phys Condens Matter 2012; 24: 424208.
203. Hamada, I, Otani, M. Comparative van der waals density-functional study of graphene on metal surfaces. Phys Rev B Cond Matter 2010; 82: 557.
204. Liu, Z, Yang, J, Grey, F et al. Observation of microscale superlubricity in graphite. Phys Rev Lett 2012; 108: 205503.
205. Wang, G, Dai, Z, Wang, Y et al. Measuring interlayer shear stress in bilayer graphene. Phys Rev Lett 2017; 119: 036101.
206. David, N, Tsvi, P, Steven, W. Statistical mechanics of membranes and surfaces. 2nd ed. Singapore, River Edge, NJ: World Scientific Pub, 2004.
207. Qin, Z, Jung, GS, Kang, MJ et al. The mechanics and design of a lightweight three-dimensional graphene assembly. Sci Adv 2017; 3: 1601536.

208. Gao, HL, Zhu, YB, Mao, LB et al. Super-elastic and fatigue resistant carbon material with lamellar multi-arch microstructure. Nat Commun 2016; 7: 12920.
209. Ma, Y, Chen, Y. Three-dimensional graphene networks: synthesis, properties and applications. Natl Sci Rev 2015; 2: 40–53.
210. Huang, X, Qi, X, Boey, F et al. Graphene-based composites. Chem Soc Rev 2011; 41: 666-86.
211. Zhang, X, Li, Q, Holesinger, TG et al. Ultrastrong, stiff, and lightweight carbon-nanotube fibers. Adv Mater 2007; 19: 4198-201.
212. Dikin, DA, Stankovich, S, Zimney, EJ et al. Graphene-Based Composite Materials. Nat 2007; 448: 457-60.
213. Kim, KH, Oh, Y, Islam, MF. Graphene coating makes carbon nanotube aerogels superelastic and resistant to fatigue. Nat Nanotechn 2012; 7: 562-66.
214. Krainyukova, NV, Zubarev, EN. Carbon honeycomb high capacity storage for gaseous and liquid species. Phys Rev Lett 2016; 116: 055501.
215. Pang, Z, Gu, X, Wei, Y et al. Bottom-up design of three-dimensional carbon-honeycomb with superb specific strength and high thermal conductivity. Nano Lett 2016; 17: 179-85.
216. Zhu, W, Low, T, Perebeinos, V et al. Structure and electronic transport in graphene wrinkles. Nano Lett 2012; 12: 3431-6.
217. Vasić, B, Zurutuza, A, Gajić, R Spatial variation of wear and electrical properties across wrinkles in chemical vapour deposition graphene. Carbon 2016; 102: 304-10.
218. Zhang, YH, Wang, B, Zhang, HR et al. The distribution of wrinkles and their effects on the oxidation resistance of chemical vapor deposition graphene. Carbon 2014; 70: 81-86.
219. Chen, S, Li, Q, Zhang, Q et al. Thermal conductivity measurements of suspended graphene with and without wrinkles by micro-Raman mapping. Nanotechn 2012; 23: 365701-4.
220. Bunch, JS, Van Der Zande, AM, Verbridge, SS et al. Electromechanical resonators from graphene sheets. Science 2007; 315: 490-3.

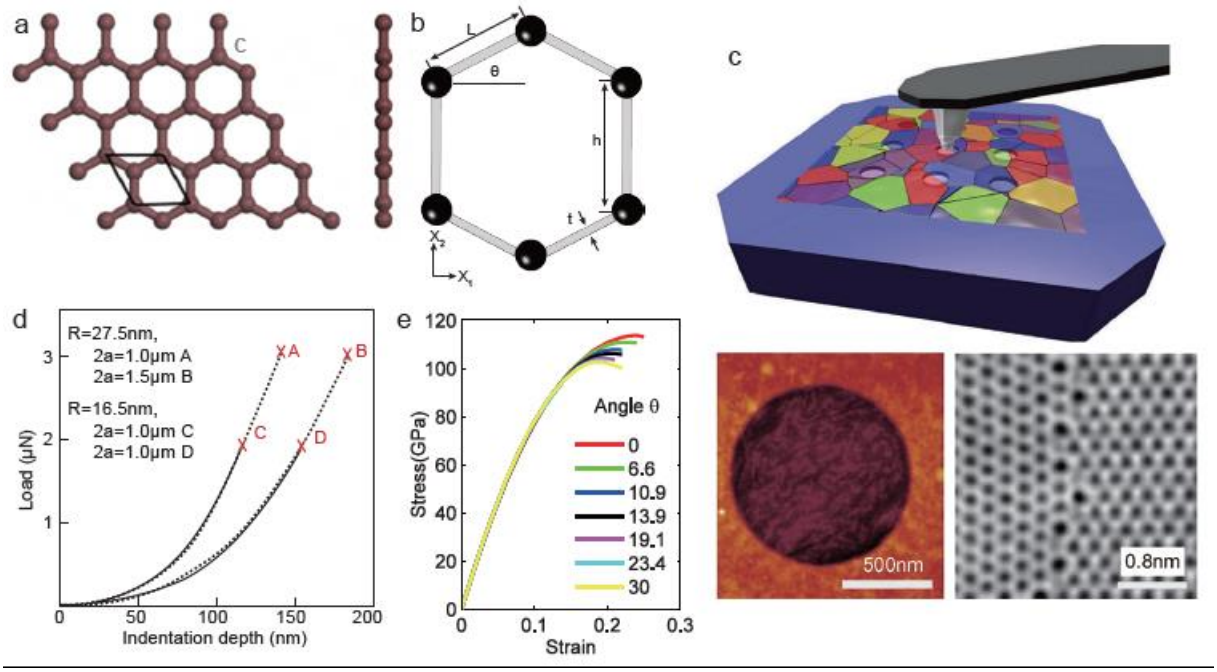

Figure 1. The stress-strain response of pristine two-dimensional materials with the hexagonal lattice. (a) Graphene lattice. (b) Continuum approximation of a honeycomb structure. (c) Sketch of using nano-indentation to measure the strength of graphene grain boundaries (GBs). The top shows the indenter on a polycrystalline graphene; bottom left shows the top view of a dent with graphene on the top and bottom right shows a graphene GB [9]. (d) Indenting load versus depth [7]. The two sets of data demonstrated that the force-displacement response is independent of the tip radius of an indenter, and the breaking force marked at each points corresponds to different loading conditions [7]. (e) The stress-strain behavior of graphene loaded with different angle θ with respect to the zigzag edge [58].

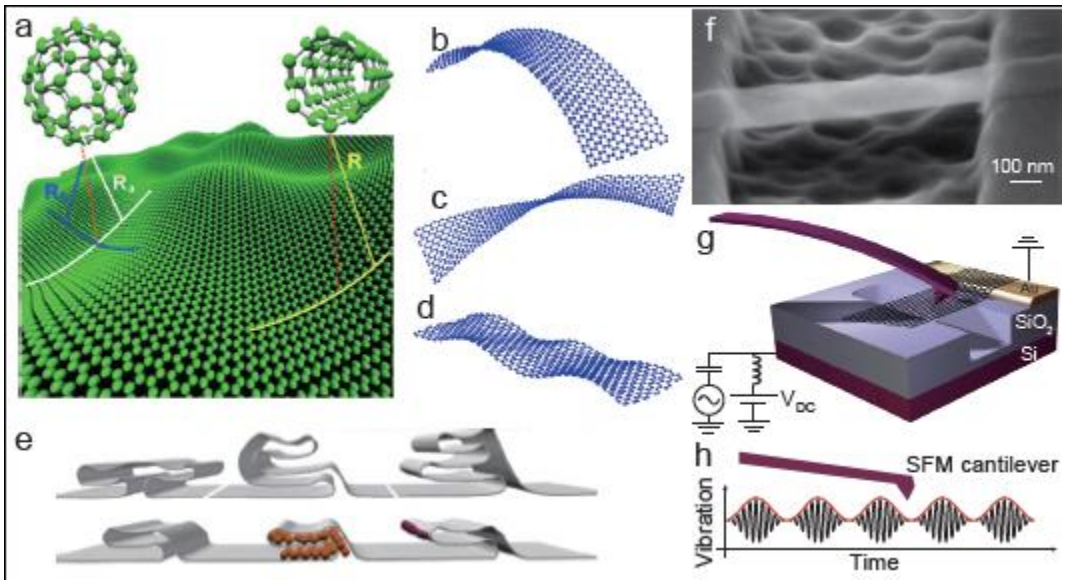

Figure 2. Governing parameters and modes of out-of-plane deformation of graphene. (a) The two governing material properties, bending rigidity and Gaussian bending stiffness, were deduced from single wall carbon nanotubes and fullerenes of different size (from [113]). (b-d) Morphology of graphene nanoribbons resulted from edge stress induced warping (reproduced from [91]). (e) Various complex folding structures [90]. (f-h) Mechanical vibrations in suspended graphene sheets [101].

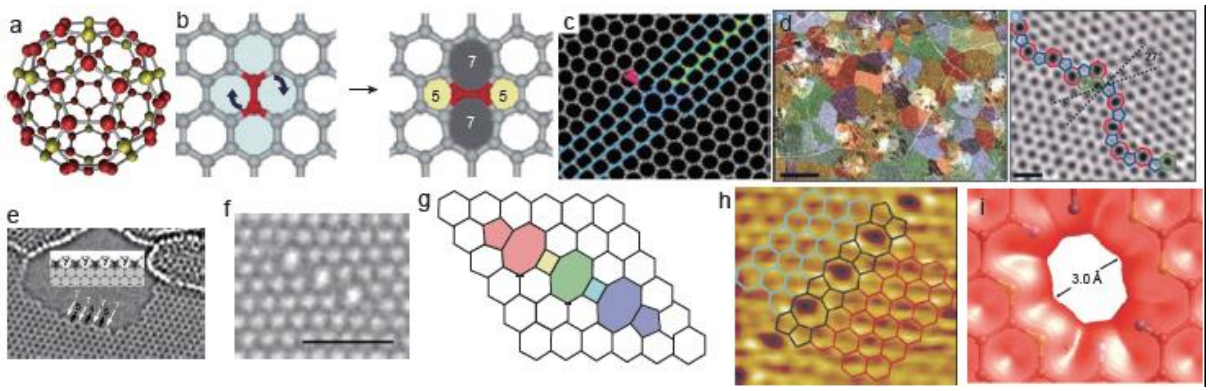

Figure 3. A variety of defects in single-layer carbon allotropes. (a) Pentagons in fullerenes (C80). (b) Stone-Thrower-Wales defect [117, 118]. (c) Observation of 5-7 defects (from [123]). (d) Grain boundaries in polycrystalline graphene (from [24]). (e) Pentagon-heptagon rings in the edge (from [80]. (f-g) 5-8 defects (from [126]): (f) The HRTEM image of 5-8 defects. Scale bar is 1 nm. (g) DFT-optimized structure of the defect for comparison with (f). (h) STM image of a linear defect (chain of two 5-rings with one 8-ring) formed in graphene epitaxial layer on Ni (111) substrate [127]. (i) Graphene-based membranes with artificial vacancies for molecular separation [128].

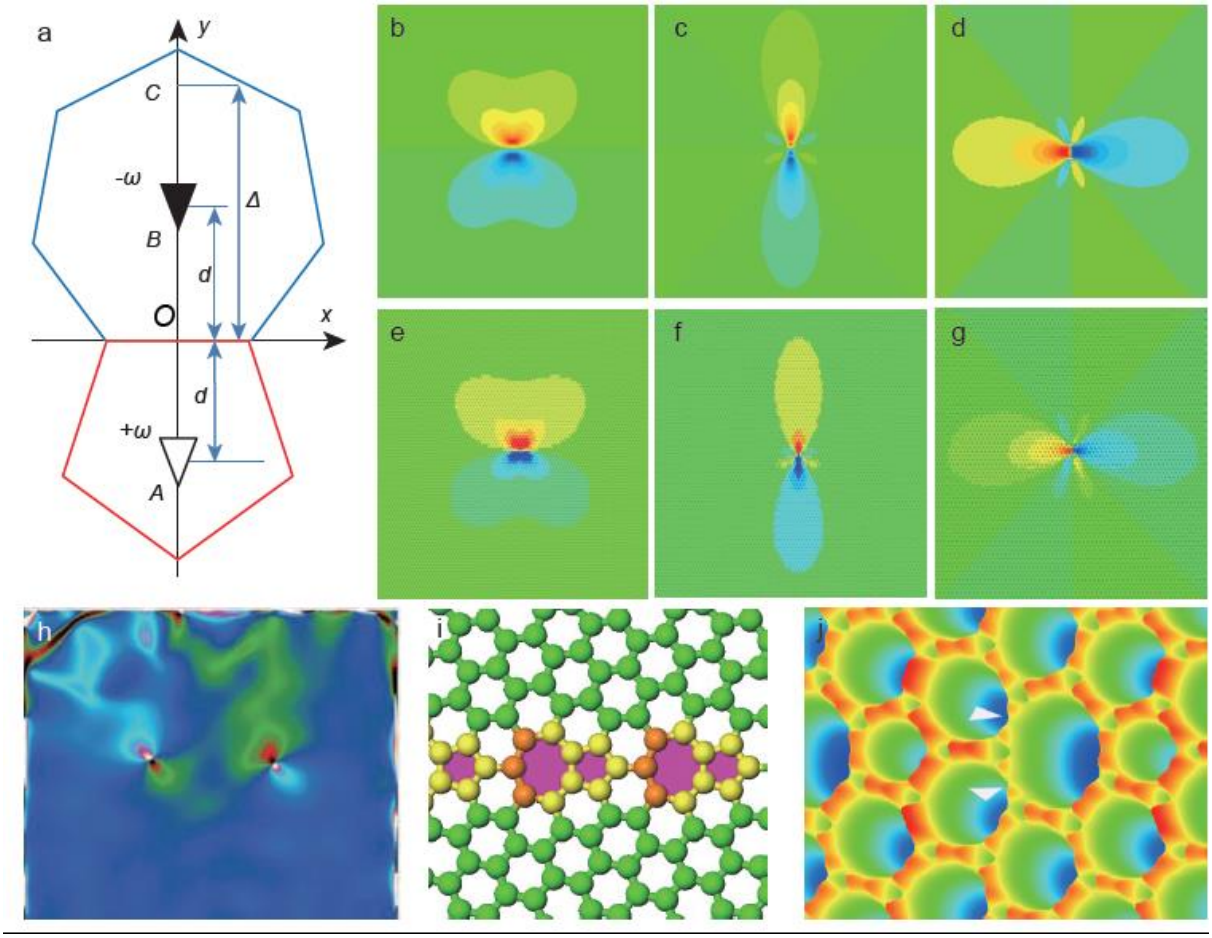

Figure 4. Stress field induced by a 5-7 defect. (a) The structure of a 5-7 ring and its equivalence to a disclination dipole. (b) to (d) The stress contours of σ_{xx}, σ_{yy}, and σ_{xy} predicted by the disclination dipole model; and e, f, and g, the corresponding contours for σ_{xx}, σ_{yy}, and σ_{xy} calculated using MD simulations. (h) Experimentally measured shear strain introduced by a 5-7 ring (Reproduced from [133]). (i)-(j) The structure used for DFT calculation and the local weakest bond (shared by the 6-7 ring) in the 5-7 defect (from [27]).

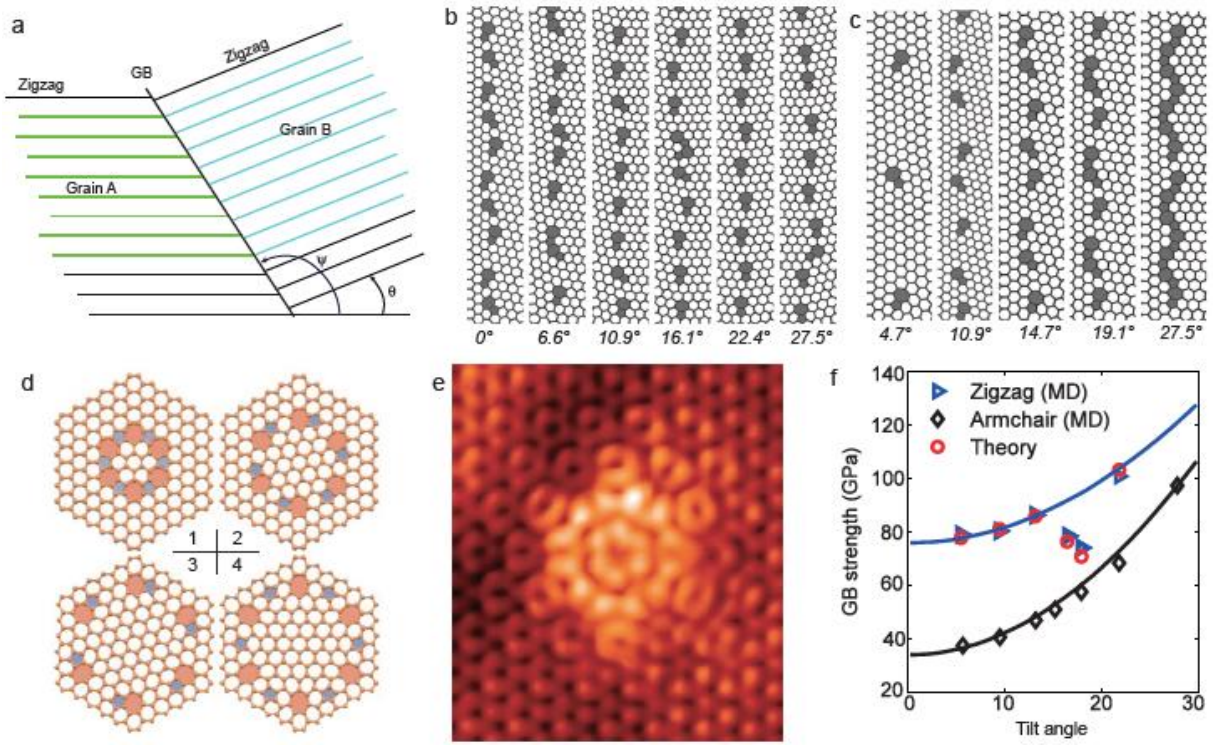

Figure 5. Grain boundary structure in a graphene sheet. (a) The two degrees of freedom in a GB in 2D materials – the misorientation θ and the GB rotation ψ. (b) Atomic structures of GBs with constant θ but different ψ from 0^o to 27.5^o. (c) GB structures with constant ψ but θ varies 4.7^o to 27.5^o (from [27]). Note GB defect density depends on θ but is insensitive to ψ. (d) and (e) Topographic images of rotational GBs (from [142]): (d) Four rotational GBs of different size (1 to 4), and (e) STM observation of type 1 GB in the epitaxial graphene on SiC. (f) The relationship of the strength vs. tilt angle (mis-orientation) of symmetrical GBs (from [26]).

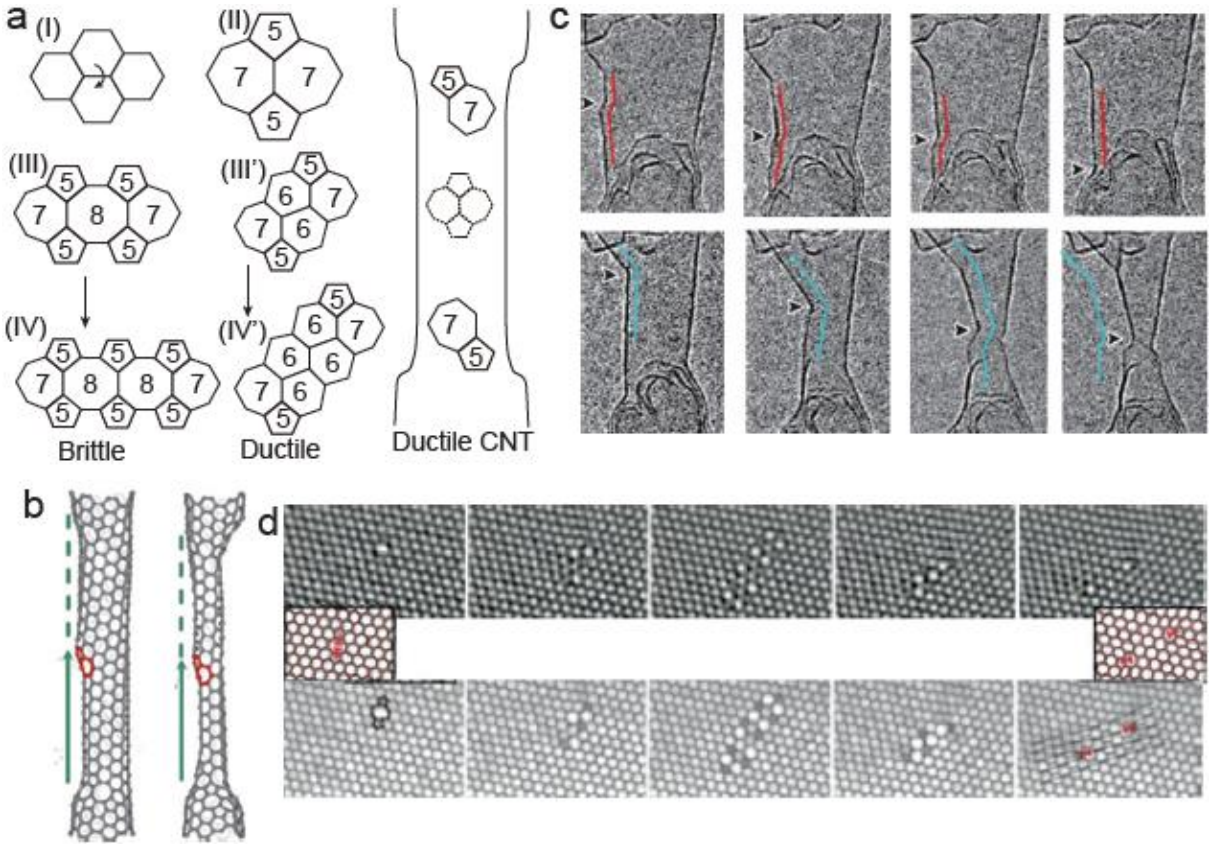

Figure 6. Motion of defects in single layer carbon allotrope. (a) Illustration to show the ductile versus brittle deformation mechanisms by the motion of 5-7 rings, (II) to (IV) for brittle and (II) to (III') and (IV') for ductile deformation (from [162]); (b) Molecular dynamics simulations to show plastic deformation mechanism in CNTs (from [163]). (c) In-situ observation of kink motion in a SWCNT under tension [165]. Sketches in the figures show the change in the shape and position of the kinks. (d) In-situ observation of defect formation, transformation and separation of a single layer graohene (from [168]).

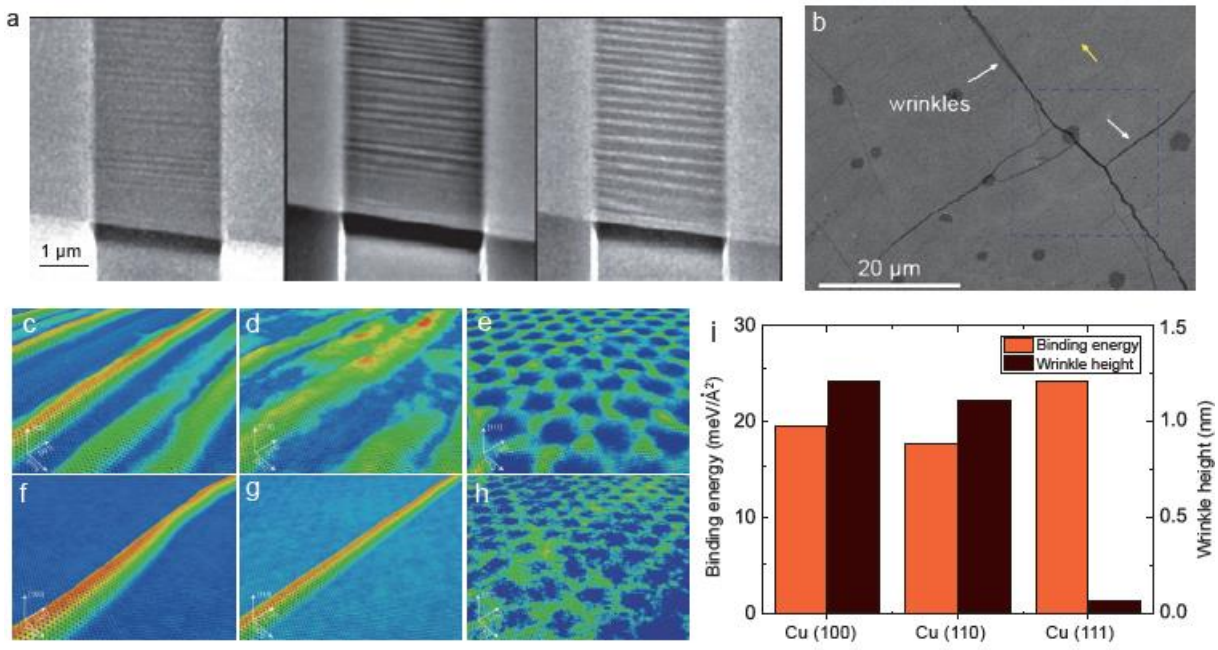

Figure 7. Wrinkling of graphene on a substrate (experiments and simulations): (a) SEM images of a membrane before annealing (left), after annealing to 425 K (middle) and to 475 K (right). Notice the increase in wavelength and amplitude of the ripples with the annealing temperature (From [183]). (b) SEM image of graphene with wrinkles on SiO_2/Si substrate (from [181]). (c-h) Morphology of graphene on Cu substrate of different crystallographic planes. (b) to (d) Morphology at 300K after initial relaxation, (c) Cu (1 0 0), (d) Cu (1 1 0), (e) Cu (1 1 1). The morphology of graphene on (f) Cu (1 0 0), (g) Cu (1 1 0), (h) Cu (1 1 1) after a sufficiently long period. Color reflects the height of wrinkles. (i) The dependence of binding energy and wrinkles height on Cu crystallographic planes (from [181]).

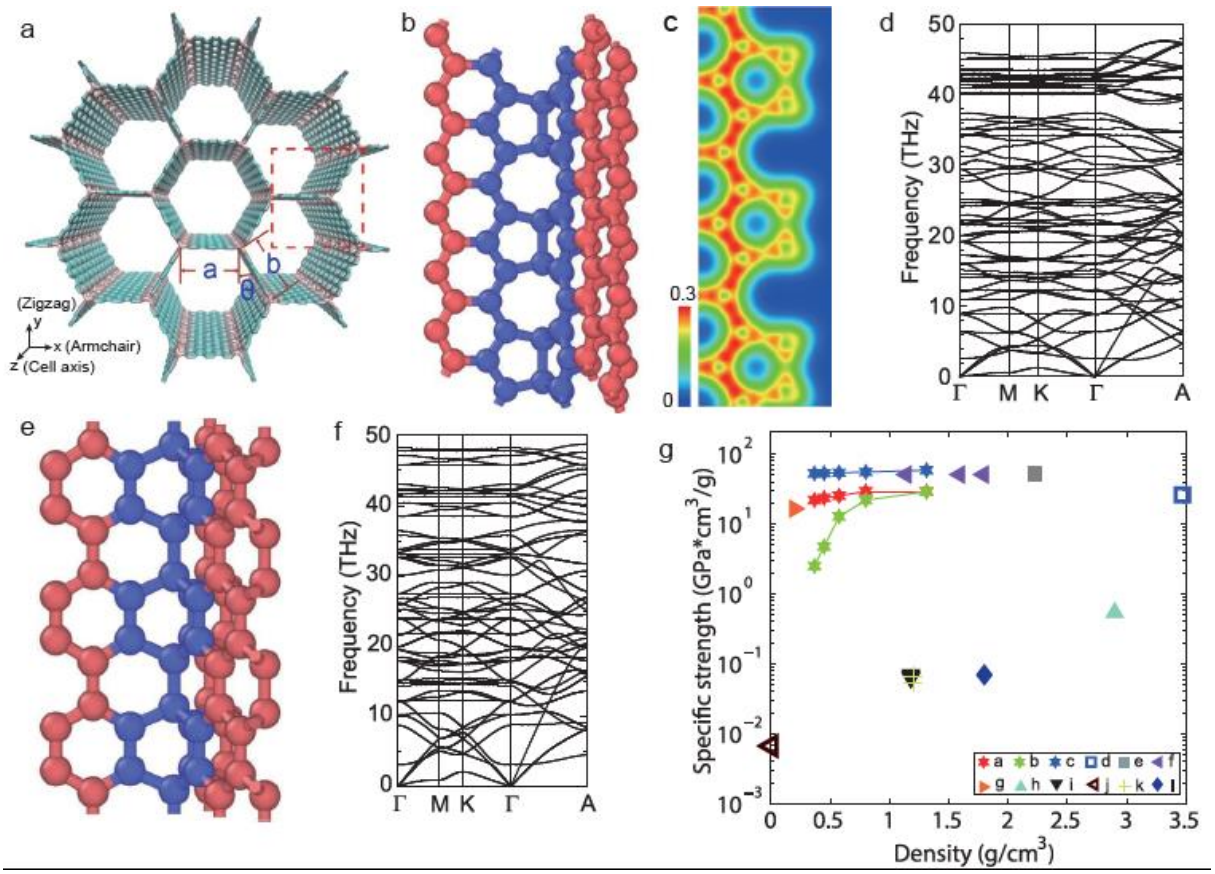

Figure 8. Stable C-honeycomb structure. (a) Atomistic structure of C-honeycomb and the coordinate system defined based on the honeycomb; (b) Local atomistic structure at the zigzag triple junction of a c-honeycomb; (c) The electron density at the junction region; (d) The phonon dispersion of the stable C-honeycomb with cell size of 5.8 Å where all phonons are with positive frequencies. (e) Local atomistic structure at the armchair triple junction of c-honeycomb; (f) The phonon dispersion of the stable C-honeycomb with cell size of 5.2 Å where all phonons are with positive frequencies. (g) Specific strength of C-honeycomb of different cell sizes and other carbon-based materials [215].

Table 1: Crack/loading angle, crack chirality, and the apparent fracture resistance Γ_G predicted by the Griffith criterion (obtained through fitting the strength vs. crack length curve by using eqn. (22)) and Γ_{MD} from MD simulations by calculating the energy of free edges along those particular chiralities.

Crack angle θ	0^o	7.5^o	15.9^o	22.5^o	30^o
Chirality $\boldsymbol{C}_h$(m,n)	(1,1)	(5,8)	(2,5)	(2,11)	(1,0)
Γ_G	15.9	15.1	14.0	13.5	11.0
Γ_{MD}	11.7	12.7	13.1	13.4	11.0

Table 2. The geometrical and material parameters used for Eqn. (24) to obtain the theoretical curves shown in Fig. 6f for both armchair and zigzag tilt GBs.

Name	ω	Δ	h_d	d	σ_{y0}
Units	(degree)	(a)	(a)	(a)	(GPa)
Zigzag	21.8	1.5	4.7	0.8	76
armchair	27.8	3.2	6.3	1.5	33